



Single-atom copper embedded in two-dimensional MXene toward peroxymonosulfate activation to generate singlet oxygen with nearly 100% selectivity for enhanced Fenton-like reactions

Peizhen Yang^{a,b}, Yuhan Long^{a,b}, Wenli Huang^{a,b,*}, Dongfang Liu^{a,b,*}

^a MOE Key Laboratory of Pollution Processes and Environmental Criteria, College of Environmental Science and Engineering, Nankai University, Tianjin 300350, PR China

^b Tianjin Key Laboratory of Environmental Technology for Complex Trans-Media Pollution, Nankai University, Tianjin 300350, PR China

ARTICLE INFO

Keywords:

Single-atom catalysts
MXene
Peroxymonosulfate
Singlet-oxygen
Wastewater treatment

ABSTRACT

Singlet oxygen ($^1\text{O}_2$)-dominated advanced oxidation processes has drawn widespread attention for selective oxidation of organic pollutants in complex water environments. However, the high efficiency and selectivity of $^1\text{O}_2$ generation remains challenging. Herein, we develop single-atom copper anchored on $\text{Ti}_3\text{C}_2\text{T}_x$ MXene nanosheets (Cu-SA/MXene) by molten salt etching for the generation of $^1\text{O}_2$ via peroxymonosulfate (PMS) activation. Particularly, it exhibits a high selectivity of 99.71% toward $^1\text{O}_2$ generation by activating PMS, which shows outstanding catalytic activity for multiple pollutants, and strong resistance to inorganic anions. Experimental and theoretical results reveal that the Cu single atoms with three oxygen coordination environments (Cu-O₃) are more favorable for PMS absorption and selectively adsorb the terminal oxygen of PMS to promote the generation of SO_5^\cdot , resulting in the generation of $^1\text{O}_2$. A continuous-flow wastewater system by dispersing catalysts on poly (vinylidene fluoride) membrane exhibit stable catalytic activity for polycarbonate plant wastewater treatment over 8 h.

1. Introduction

Persulfate-based advanced oxidation processes (PS-AOPs) have received extensive attention for fast degradation of recalcitrant organic pollutants from wastewater due to the generation of reactive oxygen species (ROS) [1,2]. Distinct from traditional hydroxyl radicals ($\bullet\text{OH}$, 1.8–2.8 V/NHE)-based AOPs, PS-based Fenton-like system (peroxymonosulfate (PMS) and peroxydisulfate (PDS)) can rapidly destroy a variety of organic pollutants in a wide pH range by generating highly reactive sulfate radicals (SO_4^\cdot , 2.5–3.1 V/NHE) via effective activation methods [3]. However, high concentrations of inorganic anions (e.g., Cl^- , CO_3^{2-} , HCO_3^- , and Br^-) and natural organic matter (NOM) co-existing with targeted pollutants in actual wastewater consume highly reactive radicals, thereby inhibiting the degradation kinetics of pollutants, lowering the utilization efficiency of oxidants, and generating more toxic by-products [4].

Singlet oxygen ($^1\text{O}_2$)-based nonradical PS oxidation has recently been verified as an alternative to radicals-dominated oxidation to solve

this problem owing to its higher selectivity to electron-rich organic pollutants, mild redox capacity (2.2 V/NHE), long half-life (2 μs vs. $\sim 1 \mu\text{s}$ ($\bullet\text{OH}$)), strong versatile inorganic ions resistance, broad pH tolerance, and reduction of toxic by-products [5–7]. In addition, asymmetric PMS molecules (HO-O-SO_3^-) are more easily activated to generate ROS than symmetric PDS molecules ($\text{HO-SO}_2\text{-O-O-SO}_2\text{-OH}$) [2]. To date, a large number of metal and carbon-based heterogeneous catalysts were reported to activate PMS to generate $^1\text{O}_2$, exhibiting strong resistance to inorganic anions [8–10]. For example, Chen and co-workers demonstrated that $^1\text{O}_2$ -dominated Fe/O-doped g-C₃N₄/PMS system can effectively degrade bisphenol A (BPA) even in the presence of eight inorganic anions (SO_4^{2-} , HCO_3^- , NO_3^- , H_2PO_4^- , CO_3^{2-} , NO_2^- , PO_4^{3-} , and Cl^- , 200 mM). Luo and co-workers also reported that excellent performance on BPA degradation was achieved in nitrogen-doped graphitic carbon/PMS system in the presence of co-existing inorganic anions with high concentrations (Cl^- , HCO_3^- , NO_3^- , and H_2PO_4^- , 500 mM). Although these reported catalysts can activate PMS to generate $^1\text{O}_2$ to be immune to the inhibiting effect of inorganic anions in water, the interference of radicals

* Corresponding authors at: MOE Key Laboratory of Pollution Processes and Environmental Criteria, College of Environmental Science and Engineering, Nankai University, Tianjin 300350, PR China

E-mail addresses: huangwenli@nankai.edu.cn (W. Huang), dongfangl@nankai.edu.cn (D. Liu).

<https://doi.org/10.1016/j.apcatb.2022.122245>

Received 18 October 2022; Received in revised form 11 November 2022; Accepted 29 November 2022

Available online 1 December 2022

0926-3373/© 2022 Elsevier B.V. All rights reserved.

is not completely eliminated. Inspired by this light, we reasonably speculate that if all the PMS can be converted into $^1\text{O}_2$ with nearly 100% selectivity, it will greatly improve the utilization efficiency of oxidant and the degradation performance of target pollutants in $^1\text{O}_2$ -dominated systems. However, the current bottleneck is that the poor selectivity of the PMS conversion and the quantitative low yielding of $^1\text{O}_2$. Therefore, it is crucial to exploit efficient approaches to solve this issue.

Single-atom catalysts (SACs) with atomically distributed metal centers exhibit maximum atomic utilization efficiency, exceptionally excellent selectivity, and high efficiency for catalytic reactions compared with traditional cluster catalysts or nanoparticles due to the homogeneity of active sites and the consistency of the local coordination environment in SACs [11–13]. Most recently, a variety of SACs have shown great application potential in $^1\text{O}_2$ selective generation. The isolated Co atoms anchored on nitrogen-doped carbon SACs with unique CoN_{2+2} active sites were reported to activate PMS for $^1\text{O}_2$ generation with 98.89% selectivity [14]. Subsequently, other SACs were also developed to regulate the activation pathway of PMS to selectively generate 100% $^1\text{O}_2$ for efficient removal of organic pollutants [15–19]. However, the investigation of SACs is still in its infancy in the selective generation of ROS through PMS activation. To date, the SACs reported so far to improve $^1\text{O}_2$ generation selectivity only include Co and Fe SACs, and the supports are almost all heteroatom-doped carbon supports with C-N-metal coordination, which limits the widespread application of SACs for environmental remediation [20]. MXene, as a transition-metal carbide and carbonitride (the general formula of MXene is $\text{M}_{n+1}\text{X}_n\text{T}_x$, where M represents an early transition metal, Ti, V, Mo, or Nb; X represents C or N; T_x represents surface functional groups -OH, -O, -Cl, or -F, $n = 1, 2$, or 3), was regarded as a good candidate to serve as promising substrates due to their exceptional properties, including abundant metal vacancy defects, excellent electronic conductivity, and hydrophilic surface terminal groups. Hence, it has been widely explored to confine single metal sites to catalyze different reactions, including hydrogen evolution reactions (HER) [21], Li-based batteries [22], carbon dioxide reduction (COR) [23,24], oxygen reduction reactions (ORR), and oxygen evolution reactions (OER) [25]. These studies confirmed that MXene with suitable surface defects and chemical functional groups are regarded as an ideal platform to confine isolated metal atom [26]. While single-atom sites anchoring on MXene to activate PMS for water purification have been reported [20,27], there is no report on the regulation of the PMS activation pathway to improve $^1\text{O}_2$ generation by MXene-based SACs, and the identification of active sites and the detailed ROS mechanism via PMS activation remains ambiguous.

Copper (Cu) has attracted extensive attention as an efficient catalyst for persulfate activation due to its diverse activation pathways [28,29]. Herein, a single-atom Cu embedded in MXene (Cu-SA/MXene) was prepared via Ti_3AlC_2 MAX immersion in the Lewis acidic molten salt (CuCl_2) at 900 °C. Atomically dispersed Cu single sites with O coordination on the surface of MXene can regulate the activation pathway of PMS to promote the generation of $^1\text{O}_2$. Impressively, Cu-SA/MXene could activate PMS to generate $^1\text{O}_2$ with nearly 100% selectivity (99.71%). Excellent $^1\text{O}_2$ generation in Cu-SA/MXene/PMS system exhibited rapid removal of target pollutants and strong resistance to high concentrations of inorganic anions. Density functional theory (DFT) and experimental results revealed that weakly positive Cu SACs were inclined to absorb the terminal O of the PMS molecule, resulting in $^1\text{O}_2$ generation. A continuous-flow wastewater system was constructed by dispersing catalysts on poly (vinylidene fluoride) membrane for polycarbonate plant wastewater treatment. This work will provide a simple and practical strategy to synthesize MXene-based SACs for boosting the generation of $^1\text{O}_2$, which will inspire the application of SACs in Fenton-like reactions.

2. Experimental section

2.1. Materials and reagents

Titanium aluminum carbide (Ti_3AlC_2 MAX, purity > 98%, 200 mesh) was purchased from Forsman Scientific Co., Ltd. (Beijing, China). Anhydrous cupric chloride (CuCl_2 , purity > 98%), copper powder, cuprous chloride (CuCl), Cu_2O , CuO , bisphenol A (BPA), p-chlorophenol (4-CP), sulfamethoxazole (SMX), paracetamol (APAP), ciprofloxacin (CIP), carbamazepine (CBZ), tetracycline hydrochloride (TC), tert-butyl alcohol (TBA), methanol, ethyl alcohol (EtOH), furfuryl alcohol (FFA), L-histidine (LHD), acetone, β -carotene, superoxide dismutase (SOD), potassium iodide (KI), sodium fluoride (NaF), potassium dichromate ($\text{K}_2\text{Cr}_2\text{O}_7$), 5,5-dimethyl-1-pyrrolidine-N-oxide (DMPO), 2,2,6,6-tetramethyl-4-piperidinol (TEMP), deuterium oxide (D_2O), potassium peroxymonosulfate (PMS, $\text{KHSO}_5 \bullet 0.5 \text{KHSO}_4 \bullet 0.5 \text{K}_2\text{SO}_4$, $\geq 47\%$ KHSO_5 basis), nitrobenzene (NB), benzoic acid (BA), sodium chloride (NaCl), sodium sulfate (Na_2SO_4), sodium nitrate (NaNO_3), sodium bicarbonate (NaHCO_3), sodium carbonate (Na_2CO_3), dibasic sodium phosphate (Na_2HPO_4), sodium dihydrogen phosphate (NaH_2PO_4), trisodium phosphate (Na_3PO_4), sodium fluoride (NaF), sodium bromide (NaBr), humic acid (HA), ammonium persulfate (APS), sodium thiosulfate ($\text{Na}_2\text{S}_2\text{O}_3$), hydrochloric acid (HCl, 37%), sodium periodate (NaIO_4), and sodium hydroxide (NaOH) were obtained from Aladdin Co., Shanghai, China. Argon (Ar, 99.99%) was purchased from Air Liquide. Ultrapure water with a resistivity of $18.2 \text{ M}\Omega \cdot \text{cm}^{-1}$. All chemicals used in this work were analytical grade without any purification.

2.2. Synthesis of Cu-NP/MXene catalysts with different molar ratios

Briefly, Ti_3AlC_2 MAX power (0.650 g) and calculated CuCl_2 mass (0.448, 0.896, 1.344, 1.792, and 2.24 g) were mixed with molar ratios of 1:1 to 1:5 and were ground in an agate mortar, respectively. Then, the above mixtures were transferred to a capped alumina crucible, which was loaded into a tube furnace and heat treated at fixed pyrolysis temperature 900 °C with 5 °C/min for 24 h under the protection of Ar gas. After cooling, the obtained precursors were washed by ultrapure water and anhydrous ethanol for three times. Finally, the Cu-NP/MXene powers with different molar ratios were obtained under vacuum at room temperature for 12 h.

2.3. Synthesis of Cu-NP/MXene catalysts with different pyrolysis temperatures

The synthesis process of Cu-NP/MXene at different temperatures was consistent with the above. Ti_3AlC_2 MAX power (0.650 g) and CuCl_2 (1.344 g) with 1:3 molar ratios were ground in an agate mortar, respectively. Then, the above mixture was transferred to a capped alumina crucible, which was loaded into a tube furnace and heat treated at different pyrolysis temperature (700, 800, 900, and 1000 °C) with 5 °C/min for 24 h under the protection of Ar gas. After cooling, the obtained precursors were washed by ultrapure water and anhydrous ethanol for three times. Finally, the Cu-NP/MXene powers with different pyrolysis temperatures were obtained under vacuum at room temperature for 12 h.

2.4. Synthesis of Cu-SA/MXene catalysts with different pyrolysis temperature

The synthesis of MXene-based SACs by Lewis molten salt etching method was slightly modified by the work of Huang [30] and Song et al. [20]. Briefly, Ti_3AlC_2 MAX power (0.650 g) and CuCl_2 (1.344 g) with 1:3 molar ratios were ground in an agate mortar, respectively. Then, the above mixture was transferred to a capped alumina crucible, which was loaded into a tube furnace and heat treated at fixed pyrolysis temperature (700, 800, 900, and 1000 °C) with 5 °C/min for 24 h under the

protection of Ar gas. After cooling, the obtained precursors were washed by ultrapure water and anhydrous ethanol for three times. Subsequently, the obtained precursors were soaked in 3 M HCl solution under ultrasound for 6 h to remove unstable Cu particles [20]. After that, the mixture was centrifuged at 5000 rpm for 15 min. The sediment was washed with deionized water and anhydrous ethanol until the pH above 6.8. Finally, the as-prepared SACs were obtained by vacuum freeze drying at -25°C for 48 h. The samples were labeled as Cu-SA/MXene-700, Cu-SA/MXene-800, Cu-SA/MXene-900, and Cu-SA/MXene-1000. To confirm the role of single-atom Cu in PMS activation, the as-prepared Cu-SA/MXene-900 catalysts were immersed into ammonium persulfate solution ($(\text{NH}_4)_2\text{S}_2\text{O}_8$) to remove immobilized Cu on the $\text{Ti}_3\text{C}_2\text{T}_x$ MXene surface [30], the final product was named as MXene.

2.5. Evaluation of Fenton-like reaction

All degradation experiments were performed in a batch reactor using a 200 mL conical flask under magnetic stirring at 25°C . In a typical experiment, 50 mg of catalyst (0.5 g/L) was added into 100 mL of target pollutant solution, and then the conical flask was placed in darkness for 20 min under magnetic stirring at 25°C to establish absorption-desorption equilibrium. Then, 2 mM PMS was added into the suspension. Subsequently, the pH of the solution was rapidly adjusted to desired values to initiate the reaction. The reaction solution was sampled at a certain time interval and filtered with 0.22 μm membrane filters. $\text{Na}_2\text{S}_2\text{O}_3$ solution (0.1 M) was added into the solution to avoid the continuous oxidation and the concentrations of the target pollutant were monitored. Solution pH was adjusted by H_2SO_4 (0.01 M) and NaOH (0.01 M). In the degradation experiment of BPA under high salinity conditions, the BPA solution containing the specific kinds and concentrations of inorganic ions were prepared in advance and then reused as above procedures. In the cycle experiment, the used catalyst was collected by filtration and washed with ultrapure water and anhydrous ethanol for five times. Then, the used catalyst was dried in a vacuum drying oven at 80°C for 12 h and then reused as above procedures. All above experiments were performed three times and the error bars were the standard deviation of the experimental data.

The degradation process of target pollutants by different catalysts was fitted by the pseudo first-order model and the apparent rate constant was estimated as following:

$$-\ln(C_t/C_0) = k_{\text{app}}t \quad (1)$$

Where C_0 is the initial pollutant concentration, $\text{mg}\cdot\text{L}^{-1}$, C_t is the concentration at a certain time, $\text{mg}\cdot\text{L}^{-1}$, and k_{app} is the apparent rate constants, min^{-1} .

The Arrhenius equation was used to calculate the activation energy of the BPA degradation process:

$$\ln k_{\text{app}} = \ln A - E_a/RT \quad (2)$$

In the equation, A represents the pre-exponential factor (min^{-1}), E_a represents the activation energy ($\text{kJ}\cdot\text{mol}^{-1}$), R represents the universal gas constant (8.314 J/mol/K) and T represents the solution temperature (K).

2.6. Catalytic membrane performance test

Firstly, 0.2 g of Cu-SA/MXene-900 catalyst was dispersed in 200 mL ultrapure water and stirred vigorously for 30 min. After that, the evenly dispersed solution (1 mg/mL, 200 mL) was obtained by ultrasonic for 2 h at 10°C . The solution was filtered onto the PVDF membrane under vacuum pressure. Finally, the Cu-SA/MXene-900/PVDF membrane was dried in a vacuum oven overnight at 60°C .

The municipal wastewater sample was collected from a wastewater treatment plant in Cangzhou, China ($38^{\circ}35'\text{N}$, $117^{\circ}61'\text{E}$). The detailed

composition of water samples was presented in the Table S1.

2.7. Quantitative experiments of ROS

Combined the reported rate constants of radicals ($k_{\text{NB}, \bullet\text{OH}} = 4.7 \times 10^9 \text{ M}^{-1} \text{ s}^{-1}$, $k_{\text{NB}, \text{SO}_4^{\cdot-}} < 10^6 \text{ M}^{-1} \text{ s}^{-1}$, $k_{\text{BA}, \bullet\text{OH}} = 4.2 \times 10^9 \text{ M}^{-1} \text{ s}^{-1}$, $k_{\text{BA}, \text{SO}_4^{\cdot-}} = 1.2 \times 10^9 \text{ M}^{-1} \text{ s}^{-1}$), the competition kinetics experiments were conducted by using NB (0.05 mM) and BA (0.06 mM) as probe compounds to determinate the steady-state of $\bullet\text{OH}$ and $\text{SO}_4^{\cdot-}$ according to Eqs. (3)–(6) [31,32].

$$\ln \frac{[\text{NB}]}{[\text{NB}]_0} = -k_{\text{OH}, \text{NB}} [\bullet\text{OH}]_{\text{SS}} t = -k_{\text{app}, \text{NB}} t \quad (3)$$

$$[\bullet\text{OH}]_{\text{SS}} = \frac{k_{\text{app}, \text{NB}}}{k_{\text{OH}, \text{NB}}} \quad (4)$$

$$\ln \frac{[\text{BA}]}{[\text{BA}]_0} = -(k_{\text{OH}, \text{BA}} [\bullet\text{OH}]_{\text{SS}} + k_{\text{SO}_4^{\cdot-}, \text{BA}} [\text{SO}_4^{\cdot-}]_{\text{SS}}) t = -k_{\text{app}, \text{BA}} t \quad (5)$$

$$[\text{SO}_4^{\cdot-}]_{\text{SS}} = \frac{k_{\text{app}, \text{BA}} - k_{\text{OH}, \text{BA}} [\bullet\text{OH}]_{\text{SS}}}{k_{\text{SO}_4^{\cdot-}, \text{BA}}} \quad (6)$$

FFA was adopted as the probe compound of $^1\text{O}_2$ due to its high reaction rate with $^1\text{O}_2$ ($k_{^1\text{O}_2, \text{FFA}} = 1.2 \times 10^8 \text{ M}^{-1} \text{ s}^{-1}$) [33]. Considering that FFA might react with $\bullet\text{OH}$ and $\text{SO}_4^{\cdot-}$ in this system, the second-order reaction rate constants between FFA and radicals were not negligible ($k_{\bullet\text{OH}, \text{FFA}} = 1.5 \times 10^{10} \text{ M}^{-1} \text{ s}^{-1}$, $k_{\text{SO}_4^{\cdot-}, \text{FFA}} = \sim 10^{10} \text{ M}^{-1} \text{ s}^{-1}$) [32]. The steady-state concentration of $^1\text{O}_2$ was measured by the loss of FFA (0.05 mM) according to Eqs. (7) and (8).

$$\ln \frac{[\text{FFA}]}{[\text{FFA}]_0} = -(k_{\text{OH}, \text{FFA}} [\bullet\text{OH}]_{\text{SS}} + k_{\text{SO}_4^{\cdot-}, \text{FFA}} [\text{SO}_4^{\cdot-}]_{\text{SS}} + k_{^1\text{O}_2, \text{FFA}} [^1\text{O}_2]_{\text{SS}}) t = -k_{\text{app}, \text{FFA}} t \quad (7)$$

$$[^1\text{O}_2]_{\text{SS}} = \frac{(k_{\text{app}, \text{FFA}} - k_{\text{OH}, \text{FFA}} [\bullet\text{OH}]_{\text{SS}} - k_{\text{SO}_4^{\cdot-}, \text{FFA}} [\text{SO}_4^{\cdot-}]_{\text{SS}})}{k_{^1\text{O}_2, \text{FFA}}} \quad (8)$$

where, $[\text{NB}]_t$, $[\text{BA}]_t$ and $[\text{FFA}]_t$ were the concentrations of NB, BA and FFA at time t, respectively; $[\text{NB}]_0$, $[\text{BA}]_0$ and $[\text{FFA}]_0$ represented the initial concentrations of NB, BA and FFA, respectively. $k_{\text{OH}, \text{NB}}$ was the second-order rate constants of NB with $\bullet\text{OH}$, $k_{\text{OH}, \text{BA}}$ and $k_{\text{SO}_4^{\cdot-}, \text{BA}}$ were the second-order rate constants of $\bullet\text{OH}$ and $\text{SO}_4^{\cdot-}$ with BA, respectively. $k_{^1\text{O}_2, \text{FFA}}$, $k_{\text{SO}_4^{\cdot-}, \text{FFA}}$, and $k_{\text{OH}, \text{FFA}}$ was the second-order rate constants of FFA with $^1\text{O}_2$, $\text{SO}_4^{\cdot-}$, and $\bullet\text{OH}$. $[\bullet\text{OH}]_{\text{SS}}$, $[\text{SO}_4^{\cdot-}]_{\text{SS}}$, and $[^1\text{O}_2]_{\text{SS}}$ were the steady-state concentration of $\bullet\text{OH}$, $\text{SO}_4^{\cdot-}$ and $^1\text{O}_2$, respectively. The pseudo first-order rate constants of NB ($k_{\text{app}, \text{NB}}$), BA ($k_{\text{app}, \text{BA}}$) and FFA ($k_{\text{app}, \text{FFA}}$) could be obtained from the plots of $-\ln([\text{NB}]_t/[\text{NB}]_0)$, $-\ln([\text{BA}]_t/[\text{BA}]_0)$ and $-\ln([\text{FFA}]_t/[\text{FFA}]_0)$ versus time t, respectively.

The contribution rates of various ROS were calculated based on the methods of previous work [16].

$$-\frac{dC_{\text{BPA}}}{dt} = k_{\text{overall}} t \quad (9)$$

$$R_{\text{OH}} = \frac{[\bullet\text{OH}]_{\text{SS}} k_{\text{OH}, \text{BPA}}}{k_{\text{overall}}} \quad (10)$$

$$R_{\text{SO}_4^{\cdot-}} = \frac{[\text{SO}_4^{\cdot-}]_{\text{SS}} k_{\text{SO}_4^{\cdot-}, \text{BPA}}}{k_{\text{overall}}} \quad (11)$$

$$R_{^1\text{O}_2} = 1 - R_{\text{OH}} - R_{\text{SO}_4^{\cdot-}} \quad (12)$$

Where k_{overall} was defined as the specific k by the overall degradation rate of BPA without the addition of quench agent. R_{OH} , $R_{\text{SO}_4^{\cdot-}}$, and $R_{^1\text{O}_2}$ were the relative contribution of $\bullet\text{OH}$, $\text{SO}_4^{\cdot-}$, and $^1\text{O}_2$ oxidation, respectively. $k_{\text{OH}, \text{BPA}}$ was the second-order rate constants of BPA with $\bullet\text{OH}$ ($17 \times 10^9 \text{ M}^{-1} \text{ s}^{-1}$), $k_{\text{SO}_4^{\cdot-}, \text{BPA}}$ was the second-order rate constants of

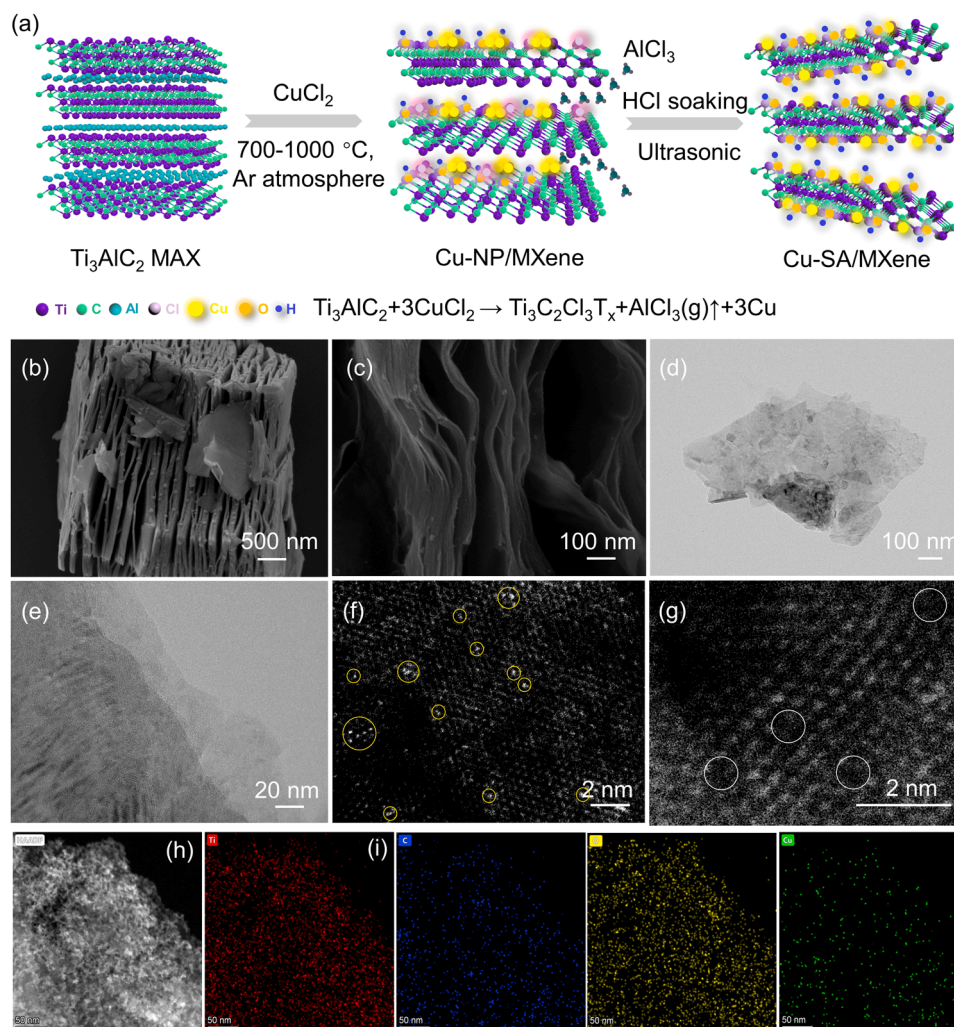


Fig. 1. Characterization of Cu-SA/MXene catalysts. (a) Schematic illustration for the synthesis of Cu-SA/MXene catalysts. (b, c) SEM images of Cu-SA/MXene-900, (d, e) TEM images of Cu-SA/MXene-900, (f, g) HAADF-STEM images of Cu-SA/MXene-900, and (h, i) the corresponding EDS elemental mappings of Ti, C, O, and Cu.

BPA with SO_4^{2-} ($1.37 \times 10^9 \text{ M}^{-1} \text{ s}^{-1}$).

The calculation process of turnover frequency (TOF) [34].

$$\text{TOF} = \frac{C_0 \times (\text{Removal efficiency } \%) }{t \times C_{\text{Cu}}} \quad (13)$$

$$C_{\text{Cu}} = \frac{C_{\text{Catalyst}} \times (\text{Cu content wt\%}) }{64} \quad (14)$$

where C_0 is the initial concentration of BPA ($\text{mol} \cdot \text{L}^{-1}$), t is the reaction time (min), C_{Cu} is the Cu element concentration ($\text{mol} \cdot \text{L}^{-1}$), C_{catalyst} is the concentration of the catalyst (g/L), $M_{\text{Cu}} = 64 \text{ g/mol}$.

3. Results and discussion

3.1. Catalyst preparation strategy and characterization

A single-atom Cu catalyst (Cu-SA/MXene) was prepared by reacting Ti_3AlC_2 MAX and CuCl_2 Lewis acidic molten salt in an Ar atmosphere (Fig. 1a). Typically, stoichiometric amounts of Ti_3AlC_2 MAX were immersed in molten CuCl_2 ($T_{\text{melting}} = 498\text{ }^\circ\text{C}$) at high pyrolysis temperatures, and the Al atoms bonded to the Ti atoms were oxidized to Al (III), forming the AlCl_3 gas phase ($T_{\text{boiling}} = 180\text{ }^\circ\text{C}$) and the reduction of Cu (II) to Cu metal. Then, the as-synthesized sample (Cu-NP/MXene) was soaked in hydrochloric acid (HCl, 3 M) under ultrasound for 6 h to remove unstable Cu metal particles. Finally, the sediment was washed

successively with water and absolute ethanol to remove residual salts, and it was denoted as Cu-SA/MXene.

In general, sufficient molten salt CuCl_2 is crucial for the removal of the Al layer in the Ti_3AlC_2 MAX precursor [35]. Therefore, the molar ratio of the initial raw material Ti_3AlC_2 MAX/ CuCl_2 (Ti_3AlC_2 MAX/ $\text{CuCl}_2 = 1:1$ – $1:5$) was investigated. X-ray diffraction (XRD) characterization demonstrated the phase evolution (Fig. S1). The Al layer of Ti_3AlC_2 MAX could not be completely etched by insufficient amount of CuCl_2 (1:1 and 1:2). As the molar ratio gradually increased to 1:3, 1:4, and 1:5, the Ti_3AlC_2 MAX phase was transformed into $\text{Ti}_3\text{C}_2\text{T}_x$ MXene, which could be confirmed in the XRD patterns that the (104) plane at 2θ 38.98° completely disappeared, (002) and (004) planes shifted from 9.89° and 19.13° to 7.91° and 15.92° . However, excessive CuCl_2 would result in a large proportion of Cu metal (JCPDS 04–0836) in the composition of the Cu-NP/MXene (1:4 and 1:5). Therefore, the appropriate Ti_3AlC_2 MAX/ CuCl_2 mole ratios should be controlled at 1:3.

In addition, the pyrolysis temperature is a key factor for SACs synthesis by molten salt etching. Too low temperature is not conducive to the etching of Al layer in Ti_3AlC_2 MAX by molten salt CuCl_2 , while too high temperature will promote the re-agglomeration of dispersed metal Cu sites to form Cu nanoparticles [36]. The scanning electron microscope (SEM) (Figs. S2a–i) and transmission electron microscopy (TEM) images (Figs. S3a, b) revealed that the Al layer of the Ti_3AlC_2 MAX precursor could not be completely etched by CuCl_2 at 700 and 800 $^\circ\text{C}$. As the pyrolysis temperature increased to 900 $^\circ\text{C}$, raw Ti_3AlC_2 MAX was

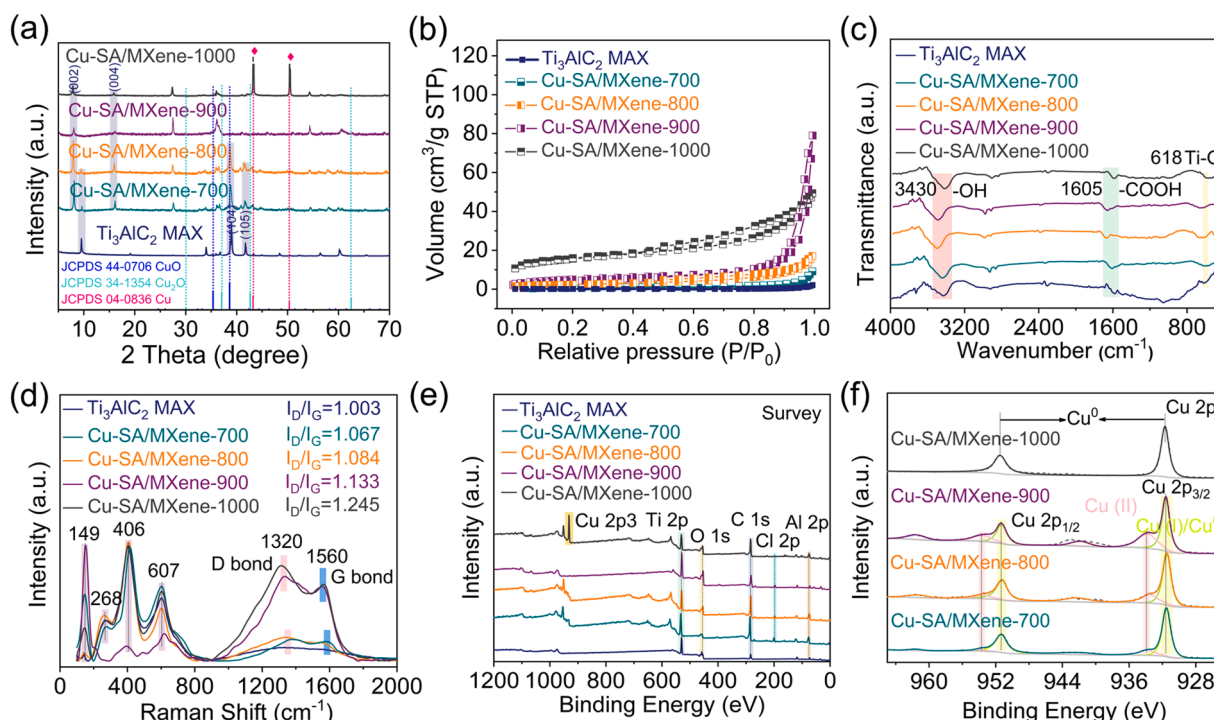


Fig. 2. Surface properties and composition of Cu-SA/MXene catalysts. (a) XRD patterns. (b) Nitrogen adsorption–desorption isotherms. (c) FT-IR Spectrometer. (d) Raman spectra. (e) XPS spectra survey of Cu-SA/MXene-700, Cu-SA/MXene-800, Cu-SA/MXene-900, and Cu-SA/MXene-1000. (f) High-resolution Cu 2p of Cu-SA/MXene-900.

transformed into a 2D layered accordion-like structure (Cu-NP/MXene-900) (Fig. S4) after reacting with molten salt CuCl_2 , which indicated that Cu nanoparticles ($\sim 0.2\text{--}0.8\ \mu\text{m}$) were anchored on the surface and interlayer of $\text{Ti}_3\text{C}_2\text{T}_x$ MXene. After soaking in HCl for 6 h with the assistance of ultrasonic, the spherical Cu nanoparticles completely disappeared, and abundant wrinkled surfaces and pores were formed (Fig. 1b, c and Figs. S2j–l). No obvious Cu particles were observed on the 2D layered $\text{Ti}_3\text{C}_2\text{T}_x$ MXene in the TEM images (Fig. 1d, e). Notably, ultrasonic dispersion promotes the formation of few-layer $\text{Ti}_3\text{C}_2\text{T}_x$ MXene nanosheets, which is beneficial to expose more active sites for catalytic reactions (Fig. S5). The 2D layered accordion-like structure of $\text{Ti}_3\text{C}_2\text{T}_x$ MXene was still well preserved at 1000°C (Figs. S2m–o). However, subsequent XRD and X-ray photoelectron spectroscopy (XPS) analyses indicated that higher temperatures (1000°C) can promote the aggregation of Cu species into zero-valent copper (Cu^0).

The aberration-corrected high-angle annular dark-field scanning TEM (AC-HAADF-STEM) was used to observe the isolated metal atoms on the support. As expected, Cu atoms were highly dispersed on $\text{Ti}_3\text{C}_2\text{T}_x$ MXene, and the bright dots within the yellow circle can be attributed to the dispersed single-atom Cu (Fig. 1f). No apparent Cu particle agglomeration was observed. Notably, Ti vacancies with strong reductivity were generated because part of the Ti atoms on the surface of $\text{Ti}_3\text{C}_2\text{T}_x$ MXene could be etched away by molten CuCl_2 (Fig. 1g), which enhanced the reduction of Cu (II) to Cu metal and the stabilization of single-atom Cu [20]. HADDF-STEM images (Fig. S6) demonstrated the difference in Cu species on Cu-NP/MXene-900 and Cu-SA/MXene-900 catalysts, revealing that both single-atom Cu and Cu nanoclusters were supported on the surface of Cu-NP/MXene-900. After 3 M HCl etching under ultrasonic environment, Cu nanoclusters were removed and only single-atom Cu remained on the surface of Cu-SA/MXene-900. The Inductively coupled plasma optical emission spectrometer (ICP-OES) test further confirmed that the Cu content of Cu-SA/MXene-900 was markedly decreased from 15.99 wt% (Cu-NP/MXene-900) to 1.19 wt% (Table S2). Meanwhile,

energy-dispersive X-ray spectroscopy (EDX) verified that Ti, C, O, and Cu atoms were uniformly distributed on the $\text{Ti}_3\text{C}_2\text{T}_x$ surface (Fig. 1h, i).

The XRD patterns (Fig. 2a) further indicated that the diffraction peaks ((104) and (105)) of Ti_3AlC_2 MAX disappeared for the Cu-SA/MXene-900. Also, the (002) peak of Ti_3AlC_2 MAX shifted toward lower angles from $2\theta\ 9.41^\circ$ to 7.62° , indicating that the interlayer spacing of Ti_3AlC_2 MAX widened owing to the replacement of Al atoms by Cu atoms [30]. The new diffraction peak at $\sim 27.2^\circ$ peak in the XRD pattern represents the (006) crystal peak of $\text{Ti}_3\text{C}_2\text{T}_x$ MXene [37]. No XRD peaks of Cu peaks, such as Cu metal (JCPDS 04–0836), Cu_2O (JCPDS 34–1354), or CuO (JCPDS 44–0706) were observed in Cu-SA/MXene-900.

The layered structure of the Cu-SA/MXene-900 had a specific Brunauer-Emmett-Teller (BET) surface area of $17.80\ \text{m}^2\cdot\text{g}^{-1}$, which was higher than that of the Ti_3AlC_2 MAX ($2.62\ \text{m}^2\cdot\text{g}^{-1}$), Cu-SA/MXene-700 ($6.58\ \text{m}^2\cdot\text{g}^{-1}$), and Cu-SA/MXene-800 ($8.26\ \text{m}^2\cdot\text{g}^{-1}$) (Fig. 2b). The average pore size of Cu-SA/MXene-900 was $\sim 5.5\ \text{nm}$ and was classified as mesoporous (Table S3, Fig. S7). For the molten salt etching method, a suitable high temperature is beneficial to the removal of the Al layer to form a multi-layer structure, which is beneficial to the subsequent adsorption and catalysis of reactants [36]. The Fourier transform infrared spectrum (FT-IR) (Fig. 2c) indicated the resonance peaks at 3430, 1605, and $618\ \text{cm}^{-1}$ were corresponding to hydroxyl groups (-OH), carbonyl group (-COOH), and titanium-oxygen covalent bond (Ti-O), respectively [27].

Raman spectroscopy was conducted to investigate the surface defect states of the prepared catalysts [38]. As shown in Fig. 2d, the strong peak intensity at $149\ \text{cm}^{-1}$ were the E_g vibrational mode of anatase phase TiO_2 particles. The Raman peak located at 268 and $607\ \text{cm}^{-1}$ were attributed to the energy gap modes of the in-plane Ti, C, and surface functional group atoms. The Raman peak located at $406\ \text{cm}^{-1}$ was assigned to the energy-gap modes of the in-plane Ti-OH and Ti-O surface functional groups. Notably, two distinct peaks at $\sim 1320\ \text{cm}^{-1}$ corresponded to D band, which represented the formation of defects of $\text{Ti}_3\text{C}_2\text{T}_x$ MXene surface and disordered graphite structure. The

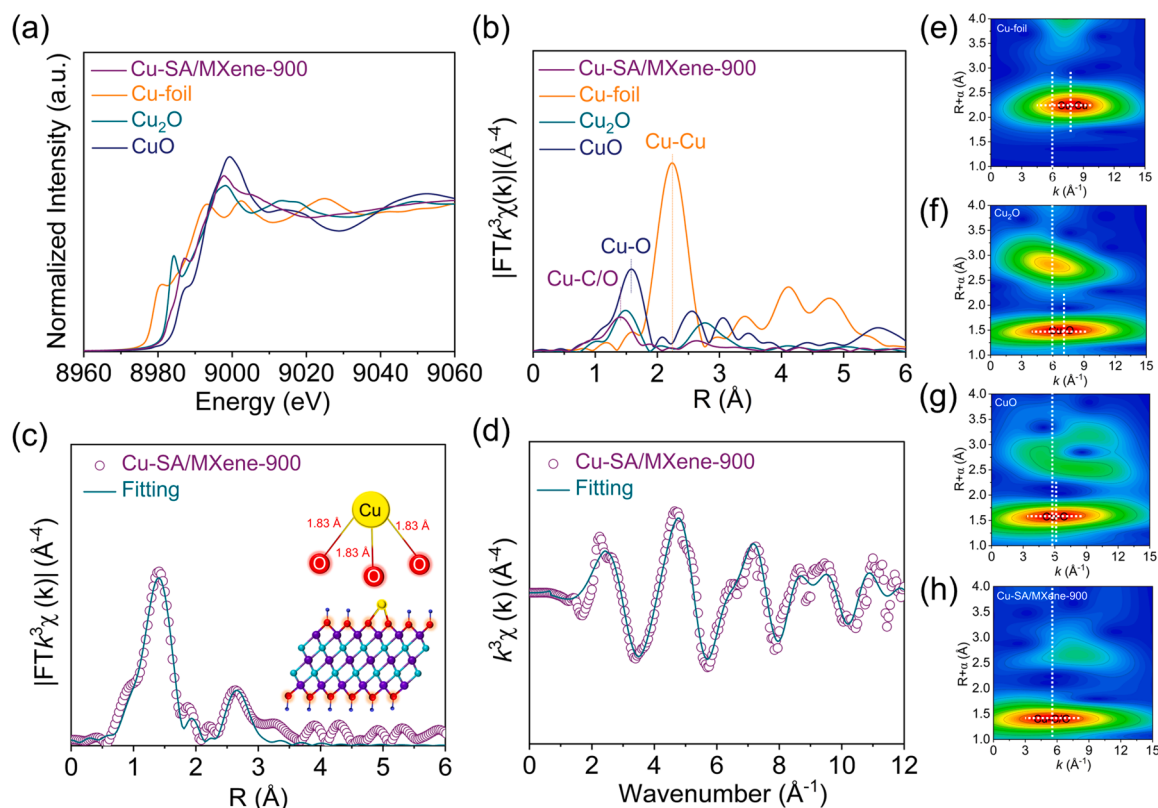


Fig. 3. Chemical state and coordination information for Cu-SA/MXene-900 catalysts. (a) Normalized XANES spectra at the Cu k -edge of Cu-SA/MXene-900, Cu-foil, Cu₂O and CuO were selected as references. (b) k^3 -weighted Fourier transform of the EXAFS spectra (FT-EXAFS) of Cu-foil, Cu₂O, CuO, and Cu-SA/MXene-900. (c), (d) Cu K-edge EXAFS fitting curve for Cu-SA/MXene-900 in R and K spaces. Wavelet transforms of the (e) Cu-foil, (f) Cu₂O, (g) CuO, and (h) Cu-SA/MXene-900.

appearance of the peak at $\sim 1560\text{ cm}^{-1}$ corresponding to G band represented the stretching of C-C bond in the carbon-based materials due to sp^2 sites [39]. The intensity ratio of the D band to the G band (I_D/I_G) was applied to present the defective degree of structural defects such as vacancies, edges and topologic defects. [40] The I_D/I_G value of Cu-SA/MXene-900 (1.133) was higher than Ti₃AlC₂ MAX (1.003), indicating that the higher pyrolysis temperature and etching processes increased the density of defects on the Ti₃C₂T_x MXene surface, which was beneficial to the stability of isolated atoms on Ti₃C₂T_x MXene [41].

The chemical compositions and elemental valences of the prepared catalysts were investigated using XPS. The survey spectra (Fig. 2e, Table S4) revealed that Ti, C, O, and Cu were the dominant elements of Cu-SA/MXene-900. The spectra of Ti 2p, C 1s and O 1s are shown in Fig. S8. The high-resolution Cu 2p spectrum of Cu-SA/MXene-900 (Fig. 2f) indicated that the two peaks located at 951.4 eV (Cu 2p_{1/2}) and 931.5 eV (Cu 2p_{3/2}) corresponded to Cu(I)/Cu⁰. The two peaks at 953.8 eV (Cu 2p_{1/2}) and 933.7 eV (Cu 2p_{3/2}) were attributed to Cu(II) [42]. Notably, the peaks at 931.4 and 951.3 eV corresponded to Cu⁰ in Cu-SA/MXene-1000, which was confirmed by Cu Auger spectroscopy (Fig. S9) and above XRD analysis (Fig. 2a).

X-ray absorption near-edge structure (XANES) and extended X-ray absorption fine structure (EXAFS) was used to explore the electronic structure and coordination environment of SACs at the Cu K-edge [43]. As shown in Fig. 3a, the near-edge absorption energy of Cu-SA/MXene-900 was located between that of the standard reference Cu₂O and CuO, indicating that the Cu valence state was between Cu(I) and Cu(II) [24,36,44]. The Fourier transform-EXAFS (FT-EXAFS) curve of Cu-SA/MXene-900 in the R space (Fig. 3b) was applied to elucidate the coordination environments of the Cu atoms anchored on Ti₃C₂T_x MXene. For Cu-SA/MXene-900, the one dominant peak at $\sim 1.42\text{ Å}$ was close to the Cu-O at 1.44 Å , which was derived from the first shell of Cu-O. Moreover, the minor peak located at 2.62 Å could be attributed to

the Cu-Ti scattering path in the higher shells, which is far from the Cu-Cl bonds (2.39 Å) [24,36,45]. Notably, no apparent Cu-Cu (2.20 Å) bonds were observed. These results demonstrate the interaction between Cu and O atoms on the surface of Ti₃C₂T_x MXene. The quantitative coordination configuration of Cu-SA/MXene-900 was determined by EXAFS curve fitting (Table S5, Fig. S10). The coordination number of the Cu center with the surrounding O atoms was 3.1 ± 0.8 , and the mean bond length of Cu-O was $1.83 \pm 0.01\text{ Å}$ [24,27,46]. The Cu K-edge EXAFS fitting of the first shell in the R space (Fig. 3c) was performed following the Cu-O scattering paths, which also matched well with the fitting results in the K space (Fig. 3d). The proposed local atomic structure of Cu is shown in the inset of Fig. 3c. The wavelet transform plot of Cu-SA/MXene-900 (Fig. 3e-h) only exhibited one maximum k at 5.02 Å^{-1} , which was distinguished from Cu-foil (7.92 Å^{-1}) (corresponding to the Cu-Cu path), Cu₂O (6.84 Å^{-1}), and CuO (6.36 Å^{-1}) (corresponding to the Cu-O path), indicating that isolated Cu atoms were dispersed in MXene [36]. Therefore, 900°C was selected as the optimal pyrolysis temperature for subsequent experiments.

3.2. Performance of catalysts in Fenton-like reactions

The catalytic activity of the prepared samples was evaluated by the degradation of BPA (one of the important industrial materials, including polycarbonate, polyester, epoxy resin, and plastics). The adsorption capacities of all Ti₃AlC₂ MAX, Ti₃C₂T_x MXene, Cu-NP/MXene-900, and Cu-SA/MXene-900 catalysts toward BPA were negligible ($<30\%$ in 20 min) (Fig. S11). As depicted in Fig. 4a, only 5.70% of BPA removal could be achieved by PMS alone within 20 min, suggesting the low oxidative ability of PMS alone (1.82 V/NHE) [47]. Pristine Ti₃AlC₂ MAX and MXene exhibited weak BPA degradations of 21.00% and 49.58% in 20 min, respectively, which indicated that the MXene support without Cu atom immobilization cannot effectively activate PMS. In addition,

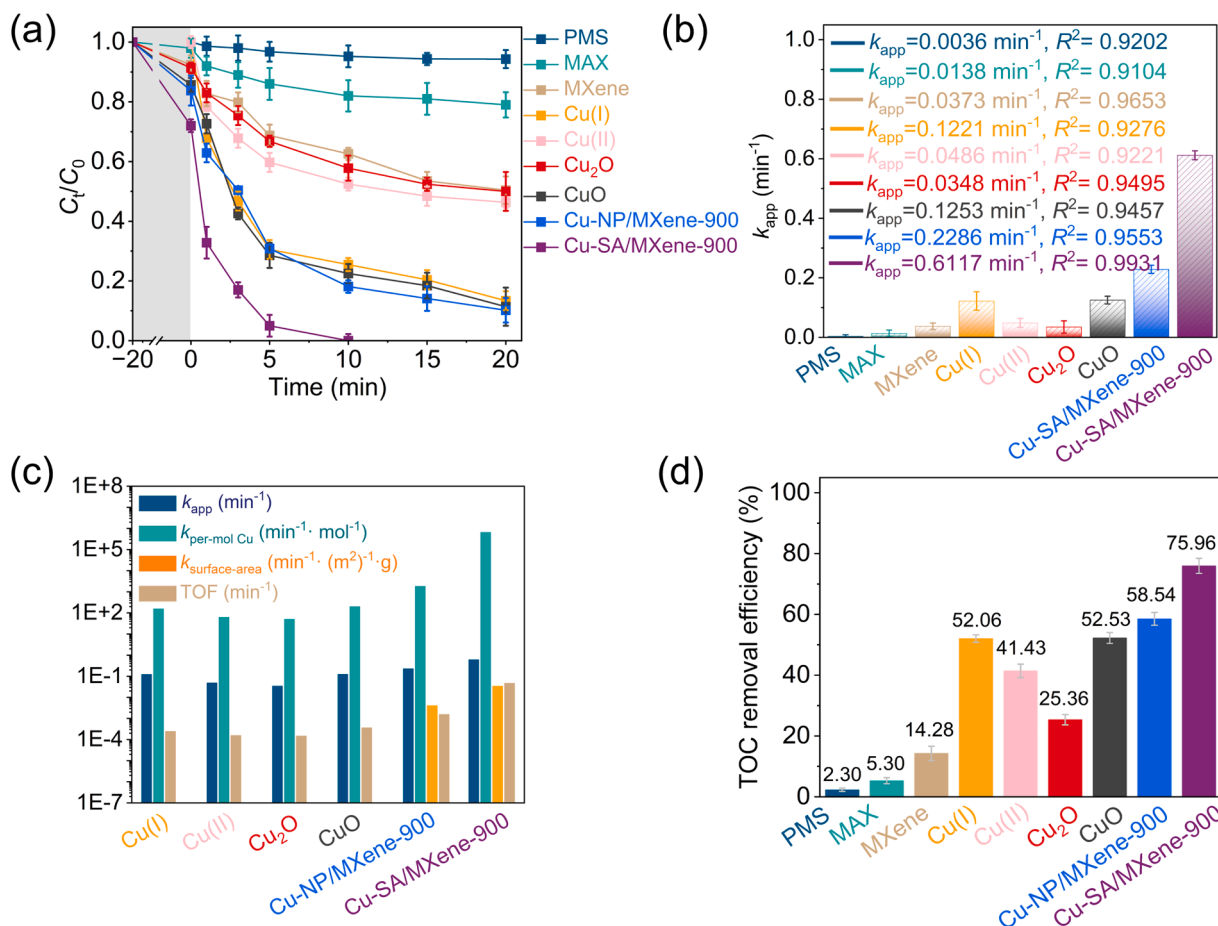


Fig. 4. Catalytic performance of prepared catalysts. (a) Degradation curves of BPA in different catalyst-activated PMS systems. (b) Apparent rate constant k_{app} of BPA in the presence of various catalysts. (c) Normalized apparent rate constant k_{app} by per mole Cu, per surface area, and TOF values. (d) Mineralization efficiency of BPA by different catalytic systems. Reaction conditions: Temperature = 298 K, initial pH = 7.0, [BPA] = 10 mg/L, [PMS] = 2.0 mM (if not otherwise specified), Catalysts = 0.5 g/L, CuCl = CuCl₂ = Cu₂O = CuO = [MAX] = [MXene] = [Cu-NP/MXene-900] = [Cu-SA/MXene-900] = 0.5 g/L.

Cu-based catalysts also exhibit unsatisfactory BPA removal due to lower catalytic activity (Fig. 4a and S12) [48,49]. Impressively, the complete removal of BPA (100%) was achieved within 10 min by Cu-SA/MXene-900 compared to 89.89% of Cu-NP/MXene-900. Previous HADDF-STEM characterizations indicated the difference in Cu active sites on the surface of Cu-NP/MXene-900 and Cu-SA/MXene-900 (Fig. S6). After etching by 3 M HCl under the ultrasonic environment, more exposed Cu single sites in Cu-SA/MXene-900 promoted the PMS activation to generate a large amount of ROS in a short time, thereby enhancing the degradation rate of the target pollutants. Besides, the degradation efficiency of Cu-SA/MXene prepared at other pyrolysis temperatures (700, 800, and 1000 °C) toward BPA was also discussed. The Cu-SA/MXene catalysts obtained at 900 °C exhibited advantages in BPA degradation over other temperatures, which can be seen from the BPA degradation process parameters (e.g., removal efficiency and k_{app}) (Fig. S12, Table S6). The possible reason is that the limited exposed Cu single sites in lower pyrolysis temperature (700 and 800 °C). However, too high pyrolysis temperature (1000 °C) will promote the agglomeration of Cu single sites into Cu metal [36]. Unfortunately, the activation capacity of Cu metal alone for PMS is weak (Fig. S13).

Meanwhile, the pseudo first-order model was used to evaluate these catalytic systems. Cu-SA/MXene-900 has achieved the highest k_{app} value (0.6117 min⁻¹), about 16 times higher than MXene (0.0373 min⁻¹) (Fig. 4b). In addition, the mineralization efficiency of target pollutants is an important evaluation parameter for the catalytic activity of catalysts. As shown in Fig. 4d, the mineralization efficiency of BPA is 75.96% in the Cu-SA/MXene-900/PMS system, which is much higher than

heterogeneous Cu-based catalysts and homogeneous Cu ions. Meanwhile, the high PMS decomposition rate (Fig. S14) also demonstrated that the Cu-SA/MXene-900 exhibited obvious advantages in the generation of active species via PMS activation. These results confirm the extraordinary catalytic activity of Cu-SA/MXene-900 as a catalyst for PMS activation.

The intrinsic properties of heterogeneous catalysts play a key role in the activation of PMS. For example, the fraction of metal components dispersed on supports and the specific surface area of the catalyst will affect the exposure ratio of active components, thus affecting the activation effect of PMS. To better understand the catalytic activity, the normalized k_{app} of the BPA degradation based on the mole ratio of metal content ($k_{per-mol\ Cu}$), surface area ($k_{surface-area}$), and turnover frequency (TOF) value were obtained [19] (Table S6). As presented in Fig. 4c, Cu-SA/MXene-900 also exhibited the highest $k_{per-mol\ Cu}$ (6.58×10^4 min⁻¹·mol⁻¹), $k_{surface-area}$ (3.44×10^{-2} min⁻¹·(m²)⁻¹·g), and TOF value (4.71×10^{-2} min⁻¹), which were higher than those of Cu-NP/MXene-900 and Cu-based catalysts, including homogeneous Cu ions and heterogeneous copper oxides. Subsequently, the TOF value of Cu-SA/MXene-900 were compared with other reported heterogeneous Fenton-like catalysts, including homogeneous Cu ions, metallic oxides, metal-supported nanoparticles, and other SACs (Table S7). Interestingly, Cu-SA/MXene-900 exhibited higher catalytic activity, which further confirmed that the MXene support can be used as an ideal support for single-atom metals to promote the decomposition of PMS to generate ROS [20].

The reusability of Cu-SA/MXene-900 was evaluated by repeating five

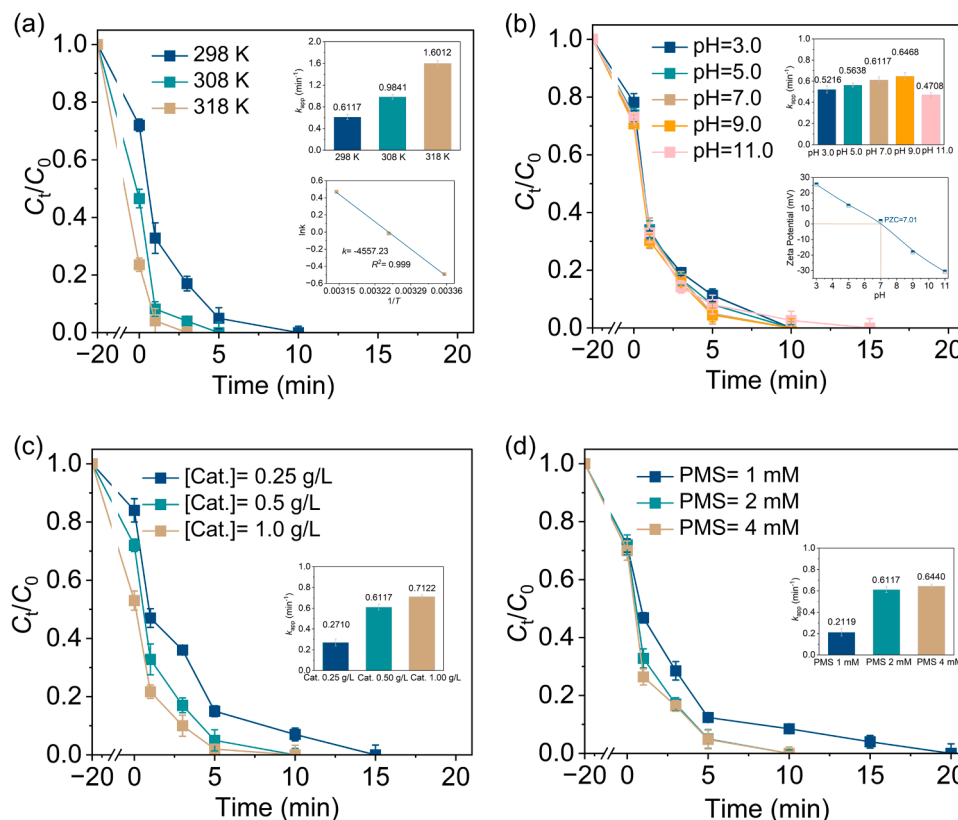


Fig. 5. Influence of reaction conditions on the performance of Fenton-like reactions. (a) Effect of temperature on the BPA degradation. (b) Effect of initial pH on the BPA degradation. (c) Effect of catalyst dosage on the BPA degradation. (d) Effect of PMS dosage on the BPA degradation. Reaction conditions: Temperature = 298–308 K, initial pH = 3.0–11.0, [BPA] = 10 mg/L, [PMS] = 1.0–4.0 mM, Catalysts = 0.25–1.0 g/L.

consecutive cycles. The degradation efficiency of BPA was maintained at > 90% in the Cu-SA/MXene-900/PMS system after five cycles (Fig. S15). Then, the Cu leaching amount of the Cu-SA/MXene-900 catalyst was determined by ICP-OES under different pH conditions (3.0–11.0). Results demonstrated that the Cu leaching of Cu-SA/MXene-900 were only 0.68, 0.45, 0.21, 0.16, and 0.08 $\mu\text{g}\cdot\text{L}^{-1}$ at different pH values (3.0–11.0), which were much lower than that of Cu-NP/MXene-900. Regardless of the initial pH, the concentrations of Cu leached from the Cu-SA/MXene-900 catalyst were far lower than the China integrated wastewater discharge standard (0.5 mg/L, GB8978–1996) (Fig. S16). Further, the residual Cu element in stable Cu-SA/MXene-900 catalyst was 0.96 wt% after five cycles, which was 80.67% of that in the fresh catalyst. The above results confirm that Cu-SA/MXene-900 has good stability as a highly efficient PMS activator.

Furthermore, the role of various operating parameters in the BPA degradation was explored. As shown in Fig. 5a, the BPA removal efficiency was enhanced as the initial temperature increased. The acceleration can be attributed to the fact that higher temperature promotes the breakage of O–O bond in PMS to generate more ROS for the degradation of pollutants [47]. The activation energy of PMS activated by Cu-SA/MXene-900 calculated based on the Arrhenius equation (Eq. (2)) was 37.89 $\text{kJ}\cdot\text{mol}^{-1}$. Also, the initial solution pH exhibited limited effect on the removal of BPA in the Cu-SA/MXene-900/PMS system. As presented in Fig. 5b, Cu-SA/MXene-900 exhibited outstanding catalytic activity over a wide pH range (3.0–11.0). The degradation efficiency of BPA maintained at 100% within 10 min in the initial pH range of 3.0–9.0. The corresponding k_{app} was in the range of 0.5216–0.6468 min^{-1} . When the initial pH was increased to extreme alkaline (11.0), the degradation of BPA was slightly inhibited (100% in 15 min, $k_{app} = 0.4708 \text{ min}^{-1}$). The possible reason is that the target pollutant BPA would be converted into BPA^- , and HSO_5^- could be

converted into SO_5^{2-} due to its pK_{a2} value of 9.4. Besides, the pH_{PZC} of Cu-SA/MXene-900 is ~ 7.01 . Therefore, the charge transfer process may be inhibited due to electrostatic repulsion between SO_5^{2-} and Cu-SA/MXene-900, resulting in the inhibition of adsorption of PMS, thereby affecting the degradation of target pollutants [50]. When the dosage of PMS is fixed, increasing the dosage of catalyst will increase the ROS generation per unit time due to providing more active sites for PMS activation (Fig. 5c). Effect of PMS dosage on the catalytic reaction was shown in Fig. 5d, the removal of BPA was greatly suppressed as insufficient amount of PMS was added, the k_{app} was only 0.2119 min^{-1} . Results demonstrated blindly increasing the dosage of PMS will not lead to a linear increase in the degradation efficiency of BPA. This is attributed to the limited active sites for PMS activation [50]. Therefore, the appropriate catalyst dosage (0.5 g/L) and PMS dosage (2 mM) were used for subsequent experiments.

3.3. Identification of reactive species

Radical quenching experiments were performed to identify the dominant active species generated during the Fenton-like reactions. It can be seen from Fig. S17 that the effect of excessive radical inhibitors on the adsorption of BPA on the catalyst is negligible. Therefore, these radical inhibitors mainly affect the BPA degradation process by reacting with radicals. It could be observed from Figs. 6a and 6c that excessive TBA (2000 mM) and EtOH (2000 mM) had little effects on the degradation performance of BPA, and the k_{app} values of BPA was slightly decreased from 0.6117 min^{-1} to 0.5617 and 0.5355 min^{-1} , respectively. The addition of SOD only showed a negligible inhibition as the k_{app} of BPA decreased from 0.6117 min^{-1} to 0.5399 min^{-1} . The weak inhibition indicated that a small amount of $\cdot\text{OH}$, $\text{SO}_4^{\cdot-}$ and $\text{O}_2^{\cdot-}$ were produced in the Cu-SA/MXene-900/PMS system. Considering that

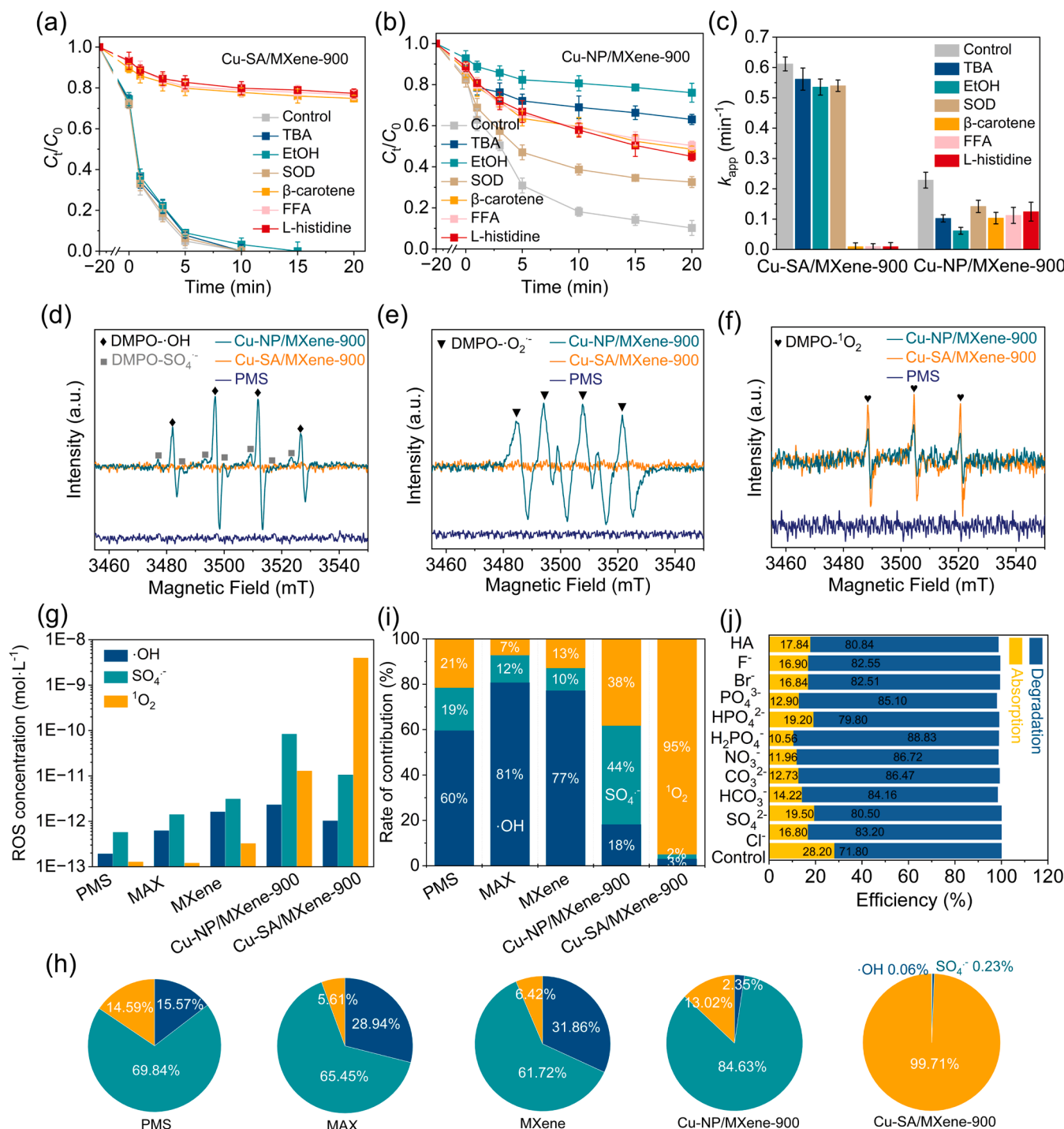


Fig. 6. Determination of ROS in Cu-NP/MXene-900 and Cu-SA/MXene-900 system. (a, b) Comparison of BPA removal efficiency of two systems in the presence of different quenchers. (c) BPA degradation rates in different quenching systems. (d-f) EPR spectra of \cdot OH, $\text{SO}_4^{\cdot-}$, $\text{O}_2^{\cdot-}$, and O_2 in two systems. (g) Steady-state concentrations of active species in different catalytic systems. (h) Proportion of ROS in different catalytic systems. (i) Contribution rate of ROS for BPA degradation in different catalytic systems. (j) Absorption and degradation efficiency of BPA contaminants in the presence of various inorganic ions at Cu-SA/MXene-900/PMS system. Reaction conditions: Temperature = 298 K, initial pH = 7.0, [BPA] = 10 mg/L, [PMS] = 2.0 mM, Catalysts = 0.5 g/L, [TBA] = [EtOH] = 2000 mM, [SOD] = 200 U·mL⁻¹, [FFA] = 20 mM, [L-histidine] = [β -carotene] = 2 mM, [DMPO] = [TEMP] = 60 mM, [Cl⁻] = [SO_4^{2-}] = [HCO_3^-] = [CO_3^{2-}] = [NO_3^-] = [H_2PO_4^-] = [HPO_4^{2-}] = [PO_4^{3-}] = [Br⁻] = [F⁻] = 200 mM, and [HA] = 10 mg/L.

common $\text{O}_2^{\cdot-}$ inhibitors, such as FFA, β -carotene, and L-histidine may interfere with the exploration of the role of $\text{O}_2^{\cdot-}$ by consuming PMS [51], the appropriate $\text{O}_2^{\cdot-}$ inhibitor concentration was determined in advance (Fig. S18). And the k_{app} of BPA were only 0.0094, 0.0097, and 0.0097 min⁻¹ in the presence of β -carotene, FFA, and L-histidine, respectively. This result demonstrated that $\text{O}_2^{\cdot-}$ was the primary ROS for

BPA degradation in Cu-SA/MXene-900/PMS system. To further confirm the presence of $\text{O}_2^{\cdot-}$ in the Cu-SA/MXene-900/PMS system, D_2O was added to the catalytic system to replace H_2O as the reaction solvent since the half-life of $\text{O}_2^{\cdot-}$ was significantly extended in D_2O (~4.2 μ s in H_2O vs ~55 μ s in D_2O) [51]. The BPA removal rate was enhanced in D_2O (Fig. S19). It further confirmed that $\text{O}_2^{\cdot-}$ is the dominant active species.

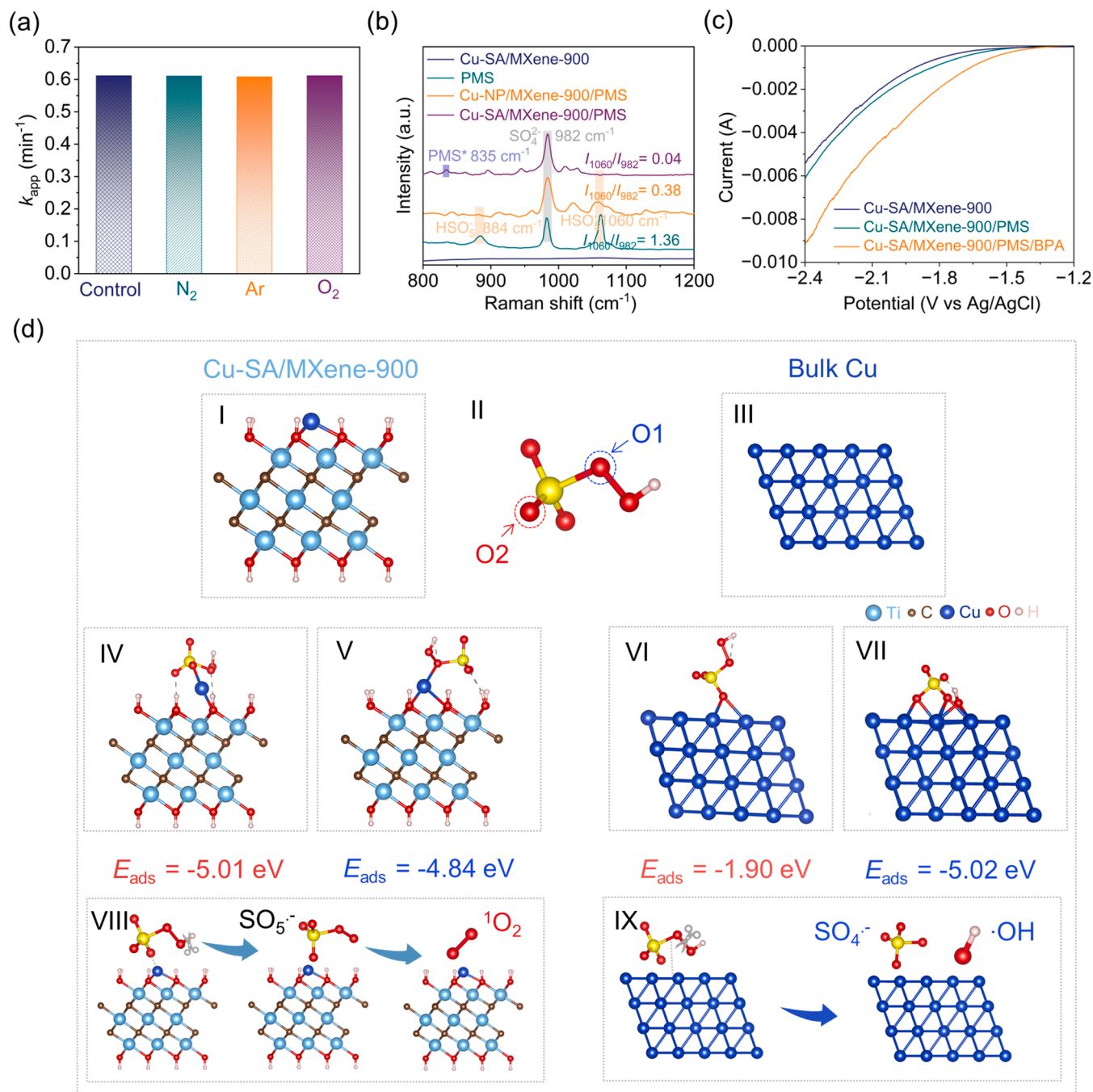


Fig. 7. Mechanism of $^1\text{O}_2$ generation by Cu-SA/MXene-900 via PMS activation. (a) Gases-saturated solutions on BPA degradation. (b) in situ Raman spectra of PMS alone, Cu-SA/MXene-900 only, Cu-NP/MXene-900/PMS, and Cu-SA/MXene-900/PMS system. (c) LSV curves of Cu-SA/MXene-900 under different conditions. (d) Optimized structure model of (I) Cu-SA/MXene-900, (II) PMS molecule, and (III) Cu-NP/MXene-900 in DFT calculations. The possible adsorption configuration (IV,V: Cu-SA/MXene-900, VI,VII: Cu-NP/MXene-900) and decomposition diagram (VIII: Cu-SA/MXene-900, IX: Cu-NP/MXene-900) of PMS on different Cu sites. Cyan, brown, red, yellow, pink and bright blue represent Ti, C, O, S and H atoms, respectively.

As for Cu-NP/MXene-900/PMS system, all quenching agents inhibited the degradation efficiency, indicating that radicals ($\cdot\text{OH}$, $\text{SO}_4^{\cdot-}$, and $\text{O}_2^{\cdot-}$) and $^1\text{O}_2$ were involved in the Cu-NP/MXene-900/PMS system (Fig. 6b and c). PMS-based AOPs always include confusing oxidation pathways such as electron transfer and surface-bound radicals. According to previous studies, other nonradical dominated oxidation processes are also immune to the addition of excessive inhibitors [52]. To further exclude the misjudgment of this work by other nonradical pathway reported by previous literatures (electron transfer and surface-bound radicals), a series of experiments were carried out to examine the nonradical

mechanism in this system. Results confirm that other nonradical processes are negligible (Fig. S20).

To verify the presence of the abovementioned ROS, EPR spectra were obtained using DMPO and TEMP as spin-trapping agents for radicals ($\cdot\text{OH}$, $\text{SO}_4^{\cdot-}$, and $\text{O}_2^{\cdot-}$) and $^1\text{O}_2$ are shown in Fig. 6d-f. Typical DMPO- $\cdot\text{OH}$, DMPO- $\text{SO}_4^{\cdot-}$, and DMPO- $\text{O}_2^{\cdot-}$ adducts were not detected in the Cu-SA/MXene-900/PMS system. The results further demonstrated that $\cdot\text{OH}$, $\text{SO}_4^{\cdot-}$, and $\text{O}_2^{\cdot-}$ were not dominant ROS in Cu-SA/MXene-900/PMS system. Moreover, a triplet signal intensity of TEMP- $^1\text{O}_2$ (1:1:1) in the Cu-SA/MXene-900/PMS system was much higher than that of the Cu-NP/

MXene-900/PMS system, indicating that single-atom Cu embedded in the $\text{Ti}_3\text{C}_2\text{Tx}$ MXene exhibited a miraculous amount of $^1\text{O}_2$ production via PMS activation.

Quantitative tests were performed to further reflect radicals and $^1\text{O}_2$ production in the PMS-based AOPs systems (Table S8, Fig. S21) [31–33]. NB, BA, and FFA were chosen as probe compounds to quantify the dominant ROS. The steady-state concentrations of $\bullet\text{OH}$, $\text{SO}_4^{\bullet-}$, and $^1\text{O}_2$ can be obtained based on Fig. S21. As shown in Fig. 6g, MXene support could not effectively activate PMS to generate ROS, and the approximately 1.60×10^{-12} M of $[\bullet\text{OH}]_{\text{ss}}$ and 1.40×10^{-12} M of $[\text{SO}_4^{\bullet-}]_{\text{ss}}$ were produced. Only 3.23×10^{-13} M of $[^1\text{O}_2]_{\text{ss}}$ was generated. For the Cu-NP/MXene-900/PMS system, the generation of ROS was improved, including 2.31×10^{-12} M of $[\bullet\text{OH}]_{\text{ss}}$, 2.32×10^{-11} M of $[\text{SO}_4^{\bullet-}]_{\text{ss}}$, and 1.28×10^{-12} M of $[^1\text{O}_2]_{\text{ss}}$. Notably, the high yield of $[^1\text{O}_2]_{\text{ss}}$ increased to 3.95×10^{-9} M and accounted for 99.71% of the total concentration of ROS produced in the Cu-SA/MXene-900/PMS system (Fig. 6h). The above results confirm that Cu single sites can effectively activate PMS and regulate the activation pathway of PMS to improve the generation and selectivity of $^1\text{O}_2$. Subsequently, the contribution rate of ROS to the BPA degradation process was calculated according to the steady-state concentration of ROS in the catalytic system. As shown in Fig. 6i, due to the high yield of $^1\text{O}_2$, its contribution rate to BPA exceeds 95% in the Cu-SA/MXene-900/PMS system, confirming the excellent degradation ability of $^1\text{O}_2$ for electrophilic organic pollutants. However, radicals are the main ROS in the MXene/PMS system, which further confirms that single-atom Cu can modulate the activation pathway of PMS to selectively generate $^1\text{O}_2$.

Inorganic anions and natural organics coexist in actual wastewater, which may interfere with the radicals-dominated AOPs [53]. To explore the strong resistance ability of $^1\text{O}_2$ -dominated Cu-SA/MXene-900/PMS system to complex environmental conditions. A variety of common high-concentration inorganic anions (Cl^- , SO_4^{2-} , HCO_3^- , CO_3^{2-} , NO_3^- , H_2PO_4^- , HPO_4^{2-} , PO_4^{3-} , Br^- , and F^- , 200 mM) and humic acids (a typical NOM, 20 mg/L) were added to the system. Interestingly, the inhibitory effects of inorganic anions with different concentrations on the Cu-SA/MXene-900/PMS system could be conquered. For instance, the degradation efficiencies of BPA were 100% (Cl^-), 100% (SO_4^{2-}), 99.45% (F^-), 99.35% (Br^-), 99.20% (CO_3^{2-}), 99.00% (HPO_4^{2-}), 98.89% (H_2PO_4^-), 98.68% (NO_3^-), 98.38% (HCO_3^-), and 98.02% (PO_4^{3-}), respectively, even the initial concentration raised to 200 mM (Fig. 6j). This further confirms the advantage of the nonradical oxidation of $^1\text{O}_2$ in the treatment of complex water bodies.

To evaluate the universal applicability of $^1\text{O}_2$ -based oxidation, multiple target contaminants, including antibiotics (sulfamethoxazole (SMX), tetracycline hydrochloride (TC), and ciprofloxacin (CIP)), phenolic compounds (p-chlorophenol (4-CP)), and PPCPs (paracetamol (APAP) and carbamazepine (CBZ)) were tested. Surprisingly, SMX, CIP, and 4-CP were completely decomposed, and the decomposition efficiencies of APAP, CBZ, and TC were > 84% within 20 min (Fig. S22a), which indicated that $^1\text{O}_2$ with moderate oxidation potential can selectively degrade electric-rich pollutants with unsaturated C=C bonds [14]. In addition, it is interesting to explore whether the dominance of $^1\text{O}_2$ is universal in degrading target pollutants with different electronic properties. Results showed that the degradation efficiencies of various target pollutants were hardly inhibited by adding excess radical inhibitor (EtOH, 2000 mM). However, the $^1\text{O}_2$ inhibitor (FFA, 20 mM) significantly inhibited the degradation of pollutants (Fig. S22b). This confirms the vital role of $^1\text{O}_2$ in the degradation of various target pollutants in the Cu-SA/MXene/PMS system. In summary, Cu single atoms immobilized by Cu-O₃ coordination on the MXene support promoted the conversion of PMS to $^1\text{O}_2$.

3.4. Possible mechanism of singlet oxygen generation

3.4.1. The source of $^1\text{O}_2$

The possible pathway toward the selective generation of $^1\text{O}_2$ in the

Cu-SA/MXene-900/PMS system was explored. First, regarding the source of $^1\text{O}_2$, there are generally three evolution pathways for $^1\text{O}_2$ generation: the self-decomposition of PMS, the contribution of O_2 , and the energy transfer of O_2 in the PMS-based oxidation process [54]. Anoxic (N_2 or Ar) and O_2 -saturated conditions exhibited negligible inhibition and promotion effects on BPA removal (Fig. 7a). Thus, the energy conversion pathway for O_2 is excluded. Negligible O_2 inhibition suggest that the generation of $^1\text{O}_2$ may not result from the recombination or disproportionation of $\text{O}_2^{\bullet-}$ (Fig. 6a and c). The self-decomposition of PMS without catalyst had little contribution to the generation of $^1\text{O}_2$ (Fig. 4a). The abovementioned results indicate that $^1\text{O}_2$ may originate from the interaction between the PMS molecules and dispersed Cu active sites on MXene.

3.4.2. Rapid adsorption of PMS molecule

The rapid adsorption of PMS molecules by heterogeneous catalysts is a critical step toward PMS activation [55]. In situ Raman spectroscopy was used to analyze the affinity of the PMS molecules for active sites. As shown in Fig. 7b, the peak at 835 cm^{-1} was related to the strong affinity between the active sites on the catalyst and PMS molecules (PMS^*). The ratio of the peak intensities at 1060 and 982 cm^{-1} (I_{1060}/I_{982}) reflects the decomposition rate of the PMS to a certain extent [3]. The ratio (I_{1060}/I_{982}) rapidly decreased from 1.36 in pure PMS to 0.04 in the Cu-SA/MXene-900/PMS system, confirming that the Cu-SA/MXene-900 accelerated the conversion of PMS molecules to ROS.

3.4.3. The direction of electron transfer

There are two possible pathways for ROS production through the activation of PMS. Electron transfer from the metal active sites to PMS molecules is a prerequisite for the generation of $\bullet\text{OH}$ and $\text{SO}_4^{\bullet-}$, accompanied by cleavage of the O-O bonds. In contrast, electron transfer from PMS molecules to the metal active sites leads to the formation of $\text{SO}_5^{\bullet-}$ and $\text{S}_2\text{O}_8^{\bullet-}$, followed by that of $\text{SO}_5^{\bullet-}$ self-reaction to generate $^1\text{O}_2$ at a fast rate ($\sim 2 \times 10^8\text{ M}^{-1}\text{ s}^{-1}$) and low activation energy ($30.93 \pm 10.03\text{ kJ}\cdot\text{mol}^{-1}$) [14,19]. Linear sweep voltammetry (LSV) analysis indicated that the current increased in the presence of PMS compared to pure Cu-SA/MXene-900 (Fig. 7c). However, the current of the Cu-NP/MXene-900/PMS system was lower than that of the Cu-NP/MXene-900 alone (Fig. S23). Charge density difference demonstrated that electrons were partly transferred from PMS to Cu-SA/MXene-900 and that electrons were transferred from bulk Cu to PMS (Fig. S24) [14]. The XPS spectra of Cu 2p are consistent with the above findings (Fig. S25). For Cu-SA/MXene-900/PMS system, the proportion of Cu(II) decreased from 42.13% to 26.40% after the reaction. However, in the Cu-NP/MXene-900/PMS system, the proportion of Cu(II) increased from 15.73% to 32.87%. These findings confirmed that the PMS molecule may act as an electron donor to transfer electrons to single-atom Cu sites to generate $^1\text{O}_2$, whereas the bulk Cu of Cu-NP/MXene-900 tends to donate electrons to the PMS molecule to generate radicals.

3.4.4. Selective adsorption of different O atoms in PMS molecule

DFT simulation calculations were used to analyze and decipher the adsorption details of PMS molecules on SACs. As shown in Fig. 7d, the oxygen atoms of PMS molecules are divided into two categories: the peroxy O atom (O1 atom) and three terminal O atoms (O2 atom) (Fig. 7d II). Previous studies have demonstrated that adsorption types, including different O atoms for binding and exposure, could lead to different PMS activation pathways, thus affecting the types of ROS [17,56–58]. Fig. 7d IV and V shows that the bonding of O2 atoms in PMS and the isolated Cu atoms is the most stable configuration, and the adsorption of O1 atoms in PMS by bulk Cu is easy to attain (Fig. 7d VI and VII). Therefore, the bulk Cu of Cu-NP/MXene-900 preferentially adsorbed O2 atoms in PMS and spontaneously decomposed into $\text{SO}_4^{\bullet-}$ and $\bullet\text{OH}$ (Fig. 7d IX). However, neither S-O nor O-O bonds were cleaved after the Cu-SA/MXene-900 adsorption of PMS. Subsequently, PMS was oxidized

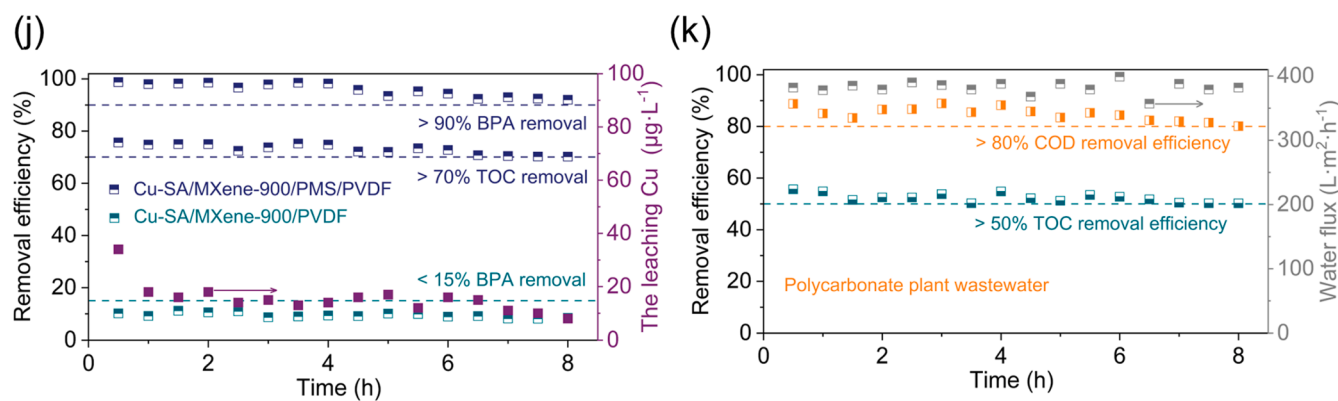
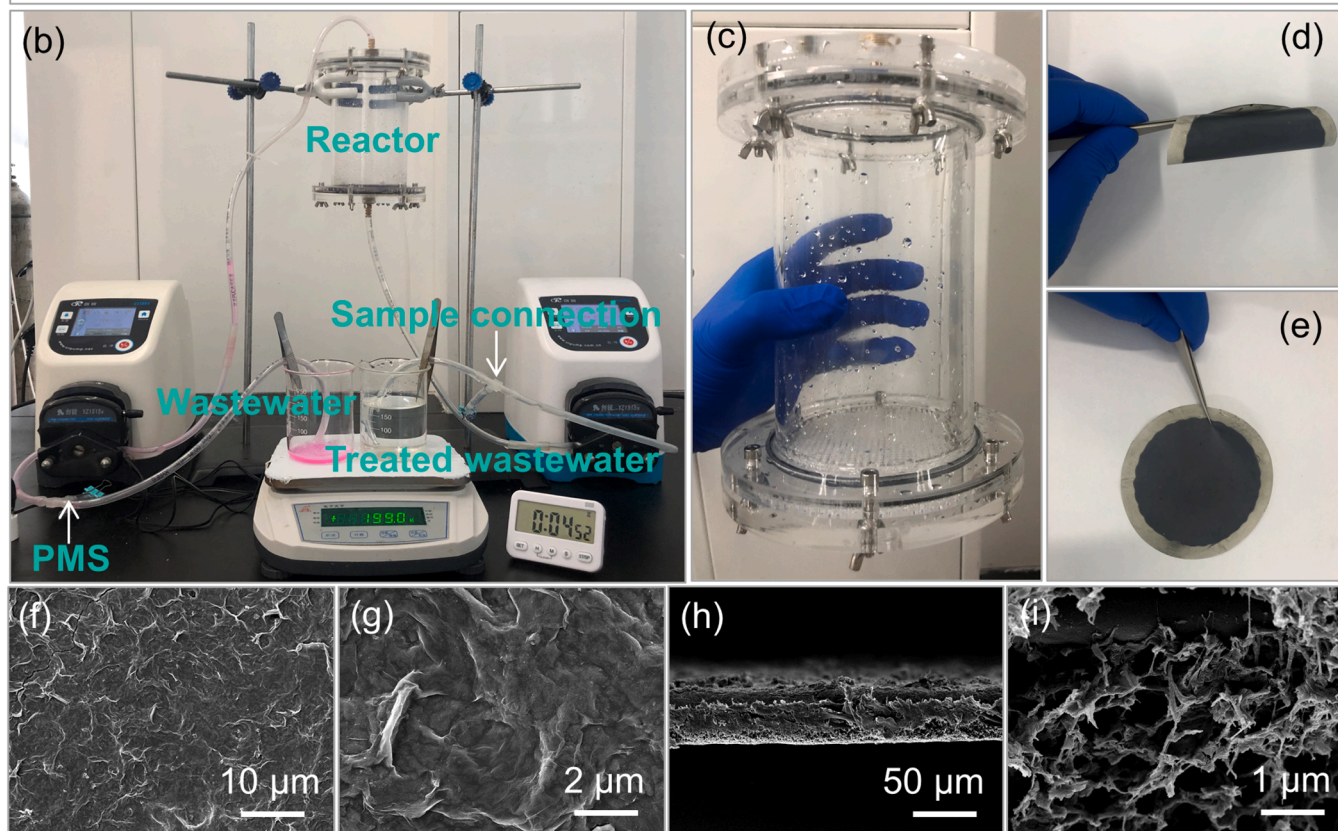
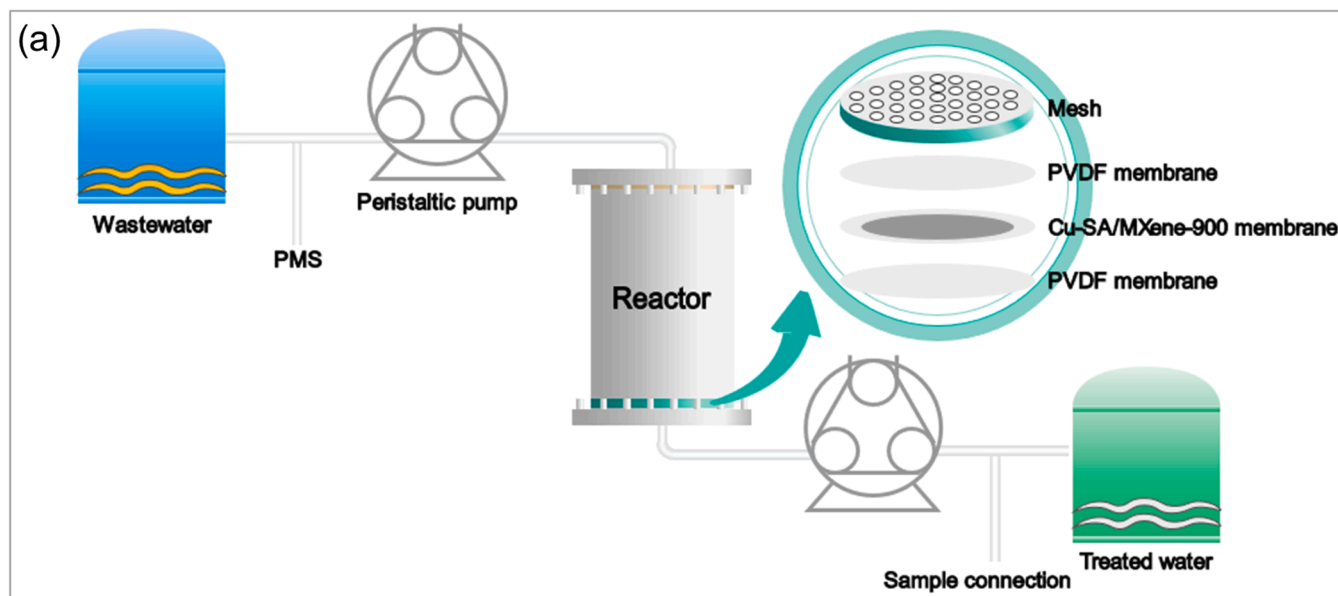
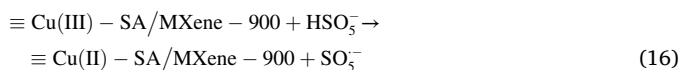


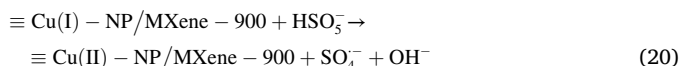
Fig. 8. Preparation of Cu-SA/MXene-900 membrane and application in actual wastewater treatment with a continuous-flow mode. (a) Schematic diagram of experimental equipment. (b, c) Photograph of experimental setup. (d, e) Cu-SA/MXene-900 membrane. (f, g) SEM images of Cu-SA/MXene-900 surface. (h, i) SEM images of Cu-SA/MXene-900 membrane cross-section. (j) BPA removal efficiency and mineralization rate in Cu-SA/MXene-900/PMS/PVDF and Cu-SA/MXene-900/PVDF systems. (k) Treatment performance of Cu-SA/MXene-900/PMS/PVDF system for polycarbonate plant wastewater. Reaction conditions: Temperature = 298 K, initial pH = 7.0, [PMS] = 2.0 mM, [BPA] = 10 mg/L, [RhB] = 10 mg/L, [COD] = 183 mg/L, and [TOC] = 58.30 mg/L.

to SO_5^- owing to the loss of H atoms because of the weak interaction between the H atom in PMS and the surface group of MXene (Fig. 7d VIII). $^1\text{O}_2$ and $\text{S}_2\text{O}_8^{2-}$ were generated through a rapid reaction between SO_5^- (Fig. S26) [14]. Recent studies have shown that high-valent Cu (Cu(III)) may contribute to the degradation of target pollutants in Fenton-like reactions [59–61]. The presence of Cu(III) in our work was confirmed by in situ Raman spectroscopy and the resulting Cu(III)-periodate complex (Fig. S27) [59]. However, the role of Cu(III) needs to be further elaborated. The high-valent Cu(III) is unstable and, therefore, its role is multiple. One is that Cu(III) with high redox potential (1.57–2.3 V/NHE) may participate in the degradation of target pollutants [60]. Also, it also accept the electrons from PMS to be reduced to form secondary radical products [61]. The oxidation contribution of Cu(III) to BPA is negligible (Fig. S28). According to this phenomenon, it is inferred that Cu(III) is highly likely to generate radicals through the reaction with PMS.

To sum up, the possible mechanism of $^1\text{O}_2$ generation by PMS activation in Cu-SA/MXene-900 was as follows Eqs. (15)–(18).



The possible radical mechanism of by PMS activation in Cu-NP/MXene-900 was as follows Eqs. (19)–(21).



3.5. Water treatment applications

To explore the potential application of the Cu-SA/MXene-900 catalyst in practical wastewater treatment, the catalyst was highly dispersed and then vacuum-filtered onto the polyvinylidene fluoride (PVDF) membrane to assemble a simple continuous-flow wastewater treatment device [62] (Fig. 8a–c). The Cu-SA/MXene-900/PVDF membrane exhibits good flexibility and intact surface (Fig. 8d–g). Fig. 8h and i demonstrated the mesh structure of the membrane cross-section after vacuum filtration, which facilitated the contact between the catalyst and the PMS oxidant to generate ROS. With Rhodamine B (RhB) as the model pollutant, the excellent catalytic performance of the Cu-SA/MXene-900/PVDF membrane can be seen from Fig. 8b. As shown in Fig. 8j, the removal efficiency of BPA was > 90% in the Cu-SA/MXene-900/PVDF/PMS system, and the mineralization efficiency of BPA was > 70% after 16 cyclic tests within 8 h. In contrast, the Cu-SA/MXene-900/PVDF system only retained < 15% of BPA removal. Moreover, the actual wastewater from the polyurethane factory was collected, and the water quality parameters are shown in Table S1. As shown in Fig. 8k, after 16 cyclic tests within 8 h, the COD removal efficiency of the actual wastewater was > 80% and the TOC removal efficiency was > 50%. Further, the water performance of the Cu-SA/MXene-900/PVDF membrane was $357\text{--}400 \text{ m}^3 \cdot \text{L}^{-1} \cdot \text{h}^{-1}$, exhibiting good separation and purification ability for the control of pollutants.

4. Conclusion

A general Lewic molten salt etching route was developed to synthesize MXene-based SACs. In contrast to the traditional C-N-metal coordination, Ti-defects-rich MXenes favor the capture and reduction of transition metal sites, resulting in the synthesized catalysts exhibiting excellent stability and reusability in Fenton-like reactions. Benefit from exposed reactive sites, Cu confined in MXene nanosheets exhibits magnificent catalytic performance for the selective generation of $^1\text{O}_2$. Particularly, Cu-SA/MXene-900 exhibit nearly 100% selectivity for $^1\text{O}_2$ generation via PMS activation, which exhibit strong resistance to pH value and high concentrations of inorganic anions. Because of the high yield of $^1\text{O}_2$, Cu-SA/MXene-900 demonstrates excellent catalytic activity for the degradation of BPA, and the TOF value reach $4.71 \times 10^{-2} \text{ min}^{-1}$, far exceeding most Cu-based Fenton-like catalysts and other SACs. Moreover, excellent $^1\text{O}_2$ generation exhibits outstanding selective oxidation for a variety of target pollutants, especially electron-rich organics. Experimental and theoretical calculation results confirm that the weakly charged Cu sites on the MXene support are beneficial to the adsorption of PMS and the selective adsorption of the terminal O of the PMS, promoting the generation of SO_5^- , resulting in the production of $^1\text{O}_2$ ($\text{PMS} \rightarrow \text{PMS}^* \rightarrow \text{SO}_5^- \rightarrow ^1\text{O}_2$). Membrane treatment system was constructed by dispersing Cu-SA/MXene-900 nanocatalysts on PVDF membrane to treat high salinity organic wastewater. After long-term operation, Cu-SA/MXene/PVDF membrane showed excellent catalytic activity in COD and TOC removal of actual wastewater. This work provides guidance for the synthesis of MXene-based SACs to modulate the PMS activation pathway for efficient removal of pollutants.

CRediT authorship contribution statement

Peizhen Yang: Investigation, Methodology, Writing – original draft. **Yuhan Long:** Software, Computation. **Wenli Huang:** Investigation, Supervision, Writing – review & editing. **Dongfang Liu:** Funding acquisition, Supervision.

Declaration of Competing Interest

The authors declare that they have no known competing financial interests or personal relationships that could have appeared to influence the work reported in this paper.

Data availability

Data will be made available on request.

Acknowledgments

This work was financially supported by the NCC Fund (NCC2020FH11). The authors would like to thank the Shiyanjia Lab (www.shiyanjia.com) for its assistance in the XAS analysis and DFT calculations.

Appendix A. Supporting information

Supplementary data associated with this article can be found in the online version at doi:10.1016/j.apcatb.2022.122245.

References

- [1] J. Lee, U. von Gunten, J.H. Kim, Persulfate-based advanced oxidation: critical assessment of opportunities and roadblocks, *Environ. Sci. Technol.* 54 (2020) 3064–3081.
- [2] X.B. Dong, B.X. Ren, Z.M. Sun, C.Q. Li, X.W. Zhang, M.H. Kong, S.L. Zheng, D. Dionysiou, Monodispersed CuFe_2O_4 nanoparticles anchored on natural kaolinite as highly efficient peroxymonosulfate catalyst for bisphenol A degradation, *Appl. Catal. B: Environ.* 253 (2019) 206–217.
- [3] Y. Chen, G. Zhang, H.J. Liu, J.H. Qu, Confining free radicals in close vicinity to contaminants enables ultrafast Fenton-like processes in the interspacing of MoS_2 membranes, *Angew. Chem. Int. Ed.* 58 (2019) 8134–8138.
- [4] J.L. Wang, S.Z. Wang, Effect of inorganic anions on the performance of advanced oxidation processes for degradation of organic contaminants, *Chem. Eng. J.* 411 (2021), 128392.
- [5] W.Y. Peng, Y.X. Dong, Y. Fu, L.L. Wang, Q.C. Li, Y.J. Liu, Q.Y. Fan, Z.H. Wang, Non-radical reactions in persulfate-based homogeneous degradation processes: a review, *Chem. Eng. J.* 421 (2021), 127818.
- [6] X.Q. Zhou, Q.D. Zhao, J. Wang, Z.L. Chen, Z.Q. Chen, Nonradical oxidation processes in PMS-based heterogeneous catalytic system: generation, identification, oxidation characteristics, challenges response and application prospects, *Chem. Eng. J.* 410 (2021), 128312.
- [7] Y.B. Ding, X.R. Wang, L.B. Fu, X.Q. Peng, C. Pan, Q.H. Mao, C.J. Wang, J.C. Yan, Nonradicals induced degradation of organic pollutants by peroxydisulfate (PDS) and peroxymonosulfate (PMS): recent advances and perspective, *Sci. Total. Environ.* 765 (2021), 142794.
- [8] R. Luo, M.Q. Li, C.H. Wang, M. Zhang, M.A.N. Khan, X.Y. Sun, J.Y. Shen, W.Q. Han, L.J. Wang, J.S. Li, Singlet oxygen-dominated non-radical oxidation process for efficient degradation of bisphenol A under high salinity condition, *Water Res.* 148 (2019) 416–424.
- [9] F. Chen, L.L. Liu, J.J. Chen, W.W. Li, Y.P. Chen, Y.J. Zhang, J.H. Wu, S.C. Mei, Q. Yang, H.Q. Yu, Efficient decontamination of organic pollutants under high salinity conditions by a nonradical peroxymonosulfate activation system, *Water Res.* 191 (2021), 116799.
- [10] Z.Y. Feng, Q.L. Tian, Q.Q. Yang, Y.B. Zhou, H.Y. Zhao, G.H. Zhao, Selectively photoelectrocatalytic reduction of oxygen to hydroxyl radical and singlet oxygen: mechanism and validation in coal wastewater, *Appl. Catal. B: Environ.* 286 (2021), 119908.
- [11] B.T. Qiao, A.Q. Wang, X.F. Yang, L.F. Allard, Z. Jiang, Y.T. Cui, J.Y. Liu, J. Li, T. Zhang, Single-atom catalysis of CO oxidation using Pt-1/FeOx, *Nat. Chem.* 3 (2011) 634–641.
- [12] Y.N. Shang, X. Xu, B.Y. Gao, S.B. Wang, X.G. Duan, Single-atom catalysis in advanced oxidation processes for environmental remediation, *Chem. Soc. Rev.* 50 (2021) 5281–5322.
- [13] X.N. Li, X. Huang, S.B. Xi, S. Miao, J. Ding, W.Z. Cai, S. Liu, X.L. Yang, H.B. Yang, J. J. Cao, J.H. Wang, Y.Q. Huang, T. Zhang, B. Liu, Single cobalt atoms anchored on porous N-doped graphene with dual reaction sites for efficient Fenton-like catalysis, *J. Am. Chem. Soc.* 140 (2018) 12469–12475.
- [14] X.Y. Mi, P.F. Wang, S.Z. Xu, L.N. Su, H. Zhong, H.T. Wang, Y. Li, S.H. Zhan, Almost 100% peroxymonosulfate conversion to singlet oxygen on single-atom CoN_2+2 sites, *Angew. Chem. Int. Ed.* 60 (2021) 4588–4593.
- [15] Y.Z. Zhang, X. Chen, C. Liang, L.F. Yin, Y. Yang, Reconstructing the coordination environment of single atomic Fe-catalysts for boosting the Fenton-like degradation activities, *Appl. Catal. B: Environ.* 315 (2022), 121536.
- [16] L.S. Zhang, X.H. Jiang, Z.A. Zhong, L. Tian, Q. Sun, Y.T. Cui, X. Lu, J.P. Zou, S. L. Luo, Carbon nitride supported high-loading Fe single-atom catalyst for activating of peroxymonosulfate to generate $\text{O}-(1,2)$ with 100% selectivity, *Angew. Chem. Int. Ed.* 60 (2021) 21751–21755.
- [17] Y. Gao, T.W. Wu, C.D. Yang, C. Ma, Z.Y. Zhao, Z.H. Wu, S.J. Cao, W. Geng, Y. Wang, Y.Y. Yao, Activity Trends and mechanisms in peroxymonosulfate-assisted catalytic production of singlet oxygen over atomic metal-N-C catalysts, *Angew. Chem. Int. Ed.* 60 (2021) 22513–22521.
- [18] X. Zhao, X. Li, Z. Zhu, W.B. Hu, H.B. Zhang, J. Xu, X. Hu, Y.T. Zhou, M. Xu, H. C. Zhang, Single-atom Co embedded in BCN matrix to achieve 100% conversion of peroxymonosulfate into singlet oxygen, *Appl. Catal. B: Environ.* 300 (2021), 120759.
- [19] Z.W. Wang, E. Almatrafi, H. Wang, H. Qin, W.J. Wang, L. Du, S. Chen, G.M. Zeng, P. Xu, Cobalt single atoms anchored on oxygen-doped tubular carbon nitride for efficient peroxymonosulfate activation: simultaneous coordination structure and morphology modulation, *Angew. Chem. Int. Ed.* 61 (2022) 2338.
- [20] H.R. Song, R. Du, Y.W. Wang, D.Y. Zu, R. Zhou, Y. Cai, F.X. Wang, Z. Li, Y.M. Shen, C.P. Li, Anchoring single atom cobalt on two-dimensional MXene for activation of peroxymonosulfate, *Appl. Catal. B: Environ.* 286 (2021), 119898.
- [21] J.Q. Zhang, Y.F. Zhao, X. Guo, C. Chen, C.L. Dong, R.S. Liu, C.P. Han, Y.D. Li, Y. Gogotsi, G.X. Wang, Single platinum atoms immobilized on an MXene as an efficient catalyst for the hydrogen evolution reaction, *Nat. Catal.* 1 (2018) 985–992.
- [22] J.A. Gu, Q. Zhu, Y.Z. Shi, H. Chen, D. Zhang, Z.G. Du, S.B. Yang, Single zinc atoms immobilized on MXene ($\text{Ti}_3\text{C}_2\text{Cl}_x$) layers toward dendrite-free lithium metal anodes, *ACS Nano* 14 (2020) 891–898.
- [23] D. Zhao, Z. Chen, W.J. Yang, S.J. Liu, X. Zhang, Y. Yu, W.C. Cheong, L.R. Zheng, F. Q. Ren, G.B. Ying, X. Cao, D.S. Wang, Q. Peng, G.X. Wang, C. Chen, MXene (Ti_3C_2) vacancy-confined single-atom catalyst for efficient functionalization of CO_2 , *J. Am. Chem. Soc.* 141 (2019) 4086–4093.
- [24] H.H. Bao, Y. Qiu, X.Y. Peng, J.A. Wang, Y.Y. Mi, S.Z. Zhao, X.J. Liu, Y.F. Liu, R. Cao, L.C. Zhou, J.Q. Ren, J.Q. Sun, J. Luo, X.P. Sun, Isolated copper single sites for high-performance electroreduction of carbon monoxide to multicarbon products, *Nat., Commun.* 12 (2021) 238.
- [25] B. Wei, Z.H. Fu, D. Legut, T.C. Germann, S.Y. Du, H.J. Zhang, J.S. Francisco, R. F. Zhang, Rational design of highly stable and active MXene-based bifunctional ORR/OER double-atom catalysts, *Adv. Mater.* 33 (2021) 2102595.
- [26] M.M. Zhang, C. Lai, B.S. Li, S.Y. Liu, D.L. Huang, F.H. Xu, X.G. Liu, L. Qin, Y.K. Fu, L. Li, H. Yi, L. Chen, MXenes as superexcellent support for confining single atom: properties, synthesis, and electrocatalytic applications, *Small* 17 (2021) 2007113.
- [27] L.M. Jin, S.J. You, Y. Yao, H. Chen, Y. Wang, Y.B. Liu, An electroactive single-atom copper anchored MXene nanohybrid filter for ultrafast water decontamination, *J. Mater. Chem., A* 9 (2021) 25964–25973.
- [28] Y.B. Ding, L.B. Fu, X.Q. Peng, M. Lei, C.J. Wang, J.Z. Jiang, Copper catalysts for radical and nonradical persulfate based advanced oxidation processes: certainties and uncertainties, *Chem. Eng. J.* 427 (2022), 131776.
- [29] X. Zhou, M.K. Ke, G.X. Huang, C. Chen, W.X. Chen, K. Liang, Y.T. Qu, J. Yang, Y. Wang, F.T. Li, H.Q. Yu, Y.E. Wu, Identification of Fenton-like active Cu sites by heteroatom modulation of electronic density, *Proc. Natl. Acad. Sci. U. S. A.* 119 (2022) 2119492119.
- [30] Y.B. Li, H. Shao, Z.F. Lin, J. Lu, L.Y. Liu, B. Duployer, P.O.A. Persson, P. Eklund, L. Hultman, M. Li, K. Chen, X.H. Zha, S.Y. Du, P. Rozier, Z.F. Chai, E. Raymundo-Pinero, Q. Huang, A general Lewis acidic etching route for preparing MXenes with enhanced electrochemical performance in non-aqueous electrolyte, *Nat. Mater.* 19 (2020) 894.
- [31] J. Liang, X.G. Duan, X.Y. Xu, K.X. Chen, Y. Zhang, L. Zhao, H. Qiu, S.B. Wang, X. D. Cao, Persulfate oxidation of sulfamethoxazole by magnetic Iron-char composites via nonradical pathways: Fe(IV) versus surface-mediated electron transfer, *Environ. Sci. Technol.* 55 (2021) 10077–10086.
- [32] Y.Z. Zhang, X. Chen, C. Liang, L.F. Yin, Y. Yang, Reconstructing the coordination environment of single atomic Fe-catalysts for boosting the Fenton-like degradation activities, *Appl. Catal. B: Environ.* 315 (2022), 121536.
- [33] Y. Yang, G. Banerjee, G.W. Brudvig, J.H. Kim, J.J. Pignatello, Oxidation of organic compounds in water by unactivated peroxymonosulfate, *Environ. Sci. Technol.* 52 (2018) 5911–5919.
- [34] G. Zhao, W.C. Li, H.Y. Zhang, W. Wang, Y.P. Ren, Single atom Fe-dispersed graphitic carbon nitride ($\text{g-C}_3\text{N}_4$) as a highly efficient peroxymonosulfate photocatalytic activator for sulfamethoxazole degradation, *Chem. Eng. J.* 430 (2022), 132937.
- [35] M. Li, J. Lu, K. Luo, Y.B. Li, K.K. Chang, K. Chen, J. Zhou, J. Rosen, L. Hultman, P. Eklund, P.O.A. Persson, S.Y. Du, Z.F. Chai, Z.R. Huang, Q. Huang, Element replacement approach by reaction with Lewis acidic molten salts to synthesize nanolaminated MAX phases and MXenes, *J. Am. Chem. Soc.* 141 (2019) 4730–4737.
- [36] Q. Zhao, C. Zhang, R.M. Hu, Z.G. Du, J.N. Gu, Y.L.S. Cui, X. Chen, W.J. Xu, Z. J. Cheng, S.M. Li, B. Li, Y.F. Liu, L. Song, S.B. Yang, Selective etching quaternary MAX phase toward single atom copper immobilized MXene ($\text{Ti}_3\text{C}_2\text{Cl}_x$) for efficient CO_2 electroreduction to methanol, *ACS Nano* 15 (2021) 4927–4936.
- [37] M. Alhabeb, K. Maleski, B. Anasori, P. Lelyukh, L. Clark, S. Sin, Y. Gogotsi, Guidelines for synthesis and processing of two-dimensional titanium carbide ($\text{Ti}_3\text{C}_2\text{T}_x$ MXene), *Chem. Mater.* 29 (2017) 7633–7644.
- [38] A. Sarycheva, Y. Gogotsi, Raman spectroscopy analysis of the structure and surface chemistry of $\text{Ti}_3\text{C}_2\text{T}_x$ MXene, *Chem. Mater.* 32 (2020) 3480–3488.
- [39] Q. Noor, S.A. Zahra, M.I. Serna, C.K. Abuoudah, M.Z. Iqbal, D. Akinwande, S. Rizwan, Silicon carbide-assisted co-existence of magnetic phases in well-optimized Ti_3SiC_2 -etched MXene, *Ceram. Int.* 46 (2020) 27419–27425.
- [40] J. Wang, X.G. Duan, J. Gao, Y. Shen, X.H. Feng, Z.J. Yu, X.Y. Tan, S.M. Liu, S. B. Wang, Roles of structure defect, oxygen groups and heteroatom doping on carbon in nonradical oxidation of water contaminants, *Water Res.* 185 (2020), 116244.
- [41] Y. Jia, L.Z. Zhang, A.J. Du, G.P. Gao, J. Chen, X.C. Yan, C.L. Brown, X.D. Yao, Defect graphene as a trifunctional catalyst for electrochemical reactions, *Adv. Mater.* 28 (2016) 9532.
- [42] Y. Bai, C.L. Liu, T.T. Chen, W.T. Li, S.S. Zheng, Y.C. Pi, Y.S. Luo, H. Pang, MXene-copper/cobalt hybrids via Lewis acidic molten salts etching for high performance symmetric supercapacitors, *Angew. Chem. Int. Ed.* 60 (2021) 25318–25322.
- [43] B.Q. Wang, C. Cheng, M.M. Jin, J. He, H. Zhang, W. Ren, J. Li, D.S. Wang, Y.D. Li, A site distance effect induced by reactant molecule matchup in single-atom catalysts for Fenton-like reactions, *Angew. Chem. Int. Ed.* 61 (2021), e202207268, <https://doi.org/10.1002/anie.202207268>.
- [44] B.H. Lee, S. Park, M. Kim, A.K. Sinha, S.C. Lee, E. Jung, W.J. Chang, K.S. Lee, J. H. Kim, S.P. Cho, H. Kim, K.T. Nam, T. Hyeon, Reversible and cooperative photoactivation of single-atom Cu/TiO_2 photocatalysts, *Nat. Mater.* 18 (2019) 620–626.
- [45] G.D. Shi, Y.L. Xie, L.L. Du, X.L. Fu, X.J. Chen, W.J. Xie, T.B. Lu, M.J. Yuan, M. Wang, Constructing Cu–C bonds in a graphdiyne-regulated Cu single-atom electrocatalyst for CO_2 reduction to CH_4 , *Angew. Chem. Int. Ed.* (2022), e202203569, <https://doi.org/10.1002/anie.202203569>.
- [46] A.M. Abdel-Maged, B. Rungtaweeworani, M. Parlinska-Wojtan, X.K. Pei, O. M. Yaghi, R.J. Behm, Highly active and stable single-atom Cu catalysts supported by a metal-organic framework, *J. Am. Chem. Soc.* 141 (2019) 5201–5210.
- [47] Y.F. Qi, J. Li, Y.Q. Zhang, Q. Cao, Y.M. Si, Z.R. Wu, M. Akram, X. Xu, Novel lignin-based single atom catalysts as peroxymonosulfate activator for pollutants degradation: role of single cobalt and electron transfer pathway, *Appl. Catal. B: Environ.* 286 (2021), 119910.
- [48] T. Cai, L.J. Bu, Y.T. Wu, S.Q. Zhou, Z. Shi, Accelerated degradation of bisphenol A induced by the interaction of EGCG and Cu(II) in Cu(II)/EGCG/peroxymonosulfate process, *Chem. Eng. J.* 395 (2020), 125134.

- [49] X.R. Zhu, Y. Zhang, W. Yan, S.J. Yang, K. Wu, G. Wang, P.K. Jin, J. Wei, Peroxymonosulfate activation by mesoporous CuO nanocage for organic pollutants degradation via a singlet oxygen-dominated pathway, *Chem. Eng. J.* 9 (2021), 106757.
- [50] L.J. Peng, X.G. Duan, Y.N. Shang, B.Y. Gao, X. Xu, Engineered carbon supported single iron atom sites and iron clusters from Fe-rich Enteromorpha for Fenton-like reactions via nonradical pathways, *Appl. Catal. B: Environ.* 287 (2021), 119963.
- [51] E.T. Yun, J.H. Lee, J. Kim, H.D. Park, J. Lee, Identifying the nonradical mechanism in the peroxymonosulfate activation process: singlet oxygenation versus mediated electron transfer, *Environ. Sci. Technol.* 52 (2018) 7032–7042.
- [52] G.X. Zhu, J.L. Zhu, X.L. Fu, Q. Liu, F.Y. Cao, Y.N. Li, Q. Qin, M.L. Jiao, Co nanoparticle-embedded N,O-codoped porous carbon nanospheres as an efficient peroxymonosulfate activator: singlet oxygen dominated catalytic degradation of organic pollutants, *Phys. Chem. Chem. Phys.* 27 (2020) 15340–15353.
- [53] P.Z. Yang, S.R. Li, X.F. Liang, X.J. An, D.F. Liu, W.L. Huang, Singlet oxygen-dominated activation of peroxymonosulfate by CuO/MXene nanocomposites for efficient decontamination of carbamazepine under high salinity conditions: performance and singlet oxygen evolution mechanism, *Sep. Purif. Technol.* 285 (2022), 120288.
- [54] Y.Y. Yao, C.H. Wang, X. Yan, H. Zhang, C.M. Xiao, J.W. Qi, Z.G. Zhu, Y.J. Zhou, X. Y. Sun, X.G. Duan, J.S. Li, Rational regulation of Co-N-C coordination for high-efficiency generation of O-1(2) toward nearly 100% selective degradation of organic pollutants, *Environ. Sci. Technol.* 56 (2022) 8833–8843.
- [55] Z.H. Wan, Z.B. Xu, Y.Q. Sun, M.J. He, D.Y. Hou, X.D. Cao, D.C.W. Tsang, Critical impact of nitrogen vacancies in nonradical carbocatalysis on nitrogen-doped graphitic biochar, *Environ. Sci. Technol.* 55 (2021) 7004–7014.
- [56] P.P. Zhang, Y.Y. Yang, X.G. Duan, Y.J. Liu, S.B. Wang, Density functional theory calculations for insight into the heterocatalyst reactivity and mechanism in persulfate-based advanced oxidation reactions, *ACS Catal.* 11 (2021) 11129–11159.
- [57] J.H. Hu, Y. Lin, Y.B. Zou, L. Lin, B. Li, X.Y. Li, Transition metal single-atom embedded on N-doped carbon as a catalyst for peroxymonosulfate activation: a DFT study, *Chem. Eng. J.* 437 (2022), 135428.
- [58] S.S. Zhu, X.J. Li, J. Kang, X.G. Duan, S.B. Wang, Persulfate activation on crystallographic manganese oxides: mechanism of singlet oxygen evolution for nonradical selective degradation of aqueous contaminants, *Environ. Sci. Technol.* 53 (2019) 307.
- [59] F. Li, Z.C. Lu, T. Li, P. Zhang, C. Hu, Origin of the excellent activity and selectivity of a single-atom copper catalyst with unsaturated Cu-N-2 sites via peroxydisulfate activation: Cu(III) as a dominant oxidizing species, *Environ. Sci. Technol.* 56 (2022) 8765–8775.
- [60] L.H. Wang, H.D. Xu, N. Jiang, Z.M. Wang, J. Jiang, T. Zhang, Trace cupric species triggered decomposition of peroxymonosulfate and degradation of organic pollutants: Cu(III) being the primary and selective intermediate oxidant, *Environ. Sci. Technol.* 54 (2020) 4686–4694.
- [61] Y. Wei, J. Miao, J.X. Ge, J.Y. Lang, C.Y. Yu, L.Z. Zhang, P.J.J. Alvarez, M.C. Long, Ultrahigh peroxymonosulfate utilization efficiency over CuO nanosheets via heterogeneous Cu(III) formation and preferential electron transfer during degradation of phenols, *Environ. Sci. Technol.* 56 (2022) 8984–8992.
- [62] Y.Z. Tan, H. Wang, L. Han, M.B. Tanis-Kanbur, M.V. Pranav, J.W. Chew, Photothermal-enhanced and fouling-resistant membrane for solar-assisted membrane distillation, *J. Membr. Sci.* 565 (2018) 254–265.